Coherent X-Ray Diffraction of Zinc Oxide Nanocrystals

MPhil/PhD Transfer Report

Steven J. Leake

London Center for Nanotechnology &
Department of Physics and Astronomy
University College London
s.leake@ucl.ac.uk

Supervisor
Prof. I. K. Robinson

May 9, 2009

Abstract

This report outlines the techniques required to obtain and interpret Coherent X-ray Diffraction (CXD) imaging measurements for crystalline materials. ZnO will be introduced as the principle material under investigation with a brief overview of research to date. Chemical Vapour Transport Deposition (CVTD) was used to synthesise ZnO nanorods, initially Scanning Electron Microscopy (SEM) determined the morphology of the ZnO and CXD was used to probe the internal structure. Applications and limitations of the CXD method are discussed. An overview of the iterative algorithm approach to overcoming the phase problem encountered in CXD and the implications for the structural reconstruction are provided. The interpretation of the resulting reconstruction of a single ZnO nanorod identified strains present. We predicted strain due to the presence of oxygen vacancies in n-type ZnO, confirmation was sought in the form of annealing, plasma treatment and metal deposition experiments designed to vary the oxygen vacancy distribution in a controlled manner. Preliminary results for both annealing and plasma treatment showed no variation in strain, deposition of Iron and subsequent annealing significantly altered the internal structure of the material (CXD) but not the morphology of the crystal (SEM).

Contents

1 Introduction

In the nanoscale regime (1-100nm) both the physical and chemical properties of materials are vastly different to those of the bulk crystalline phase. These properties can be tuned by varying crystal morphology. The result is engineered industrial materials made to specification. The importance of this has driven new techniques and methods of fabrication to be developed to understand the physical processes occurring during synthesis and the physical properties the resultant sample possesses. Currently characterisation of the morphology of these materials is dominated by electron microscopy in the form of Scanning Electron Microscopy (SEM) and Transmission Electron Microscopy (TEM). These methods have been heavily developed, SEM provides topographical surface imaging and TEM provides 2D cross sections of samples with atomic resolution. Although excellent tools in their own right they have several drawbacks; they require conductive materials, vacuum compatibility and suffer from multiple scattering, penetration depth related problems and specifically for TEM the sample preparation is lengthy and often damages the sample to an extent. A proposed alternative is CXD, this method aims to probe the internal structure of the nanocrystal by inversion of the coherent three dimensional diffraction pattern surrounding each Bragg peak [1–4]. It is applicable when the crystal size is smaller than the coherence length of the incident x-ray beam in all dimensions determined by the source and experimental focussing optics [5]. By oversampling and applying iterative algorithms [6,7] to the measured diffraction pattern the phase lost during the measurement can be retrieved. The phase describes the displacement of the electron density, and as all structural defects in crystals lead to displacements (strain fields) the technique is sensitive to them. The synthesis process can therefore be characterised and refined to produce specific properties for required applications. CXD imaging of Bragg reflections is limited to monolithic crystals; the position of the Bragg peak is determined by the crystal structure, thus interfaces between two different crystal structures or the same crystal structure at a different orientation can be independently measured. This is also applicable to buried structures, assuming the host material for the buried structure is not thick enough to scatter all of the incident x-rays.

In this case Zinc Oxide (ZnO) was investigated using CXD; it was synthesised using a well documented Chemical Vapour Transport Deposition method (CVTD) [8, 9] in nanorod form and deposited onto Silicon, Quartz, Sapphire and Indium Tin Oxide (ITO) substrates. ZnO exhibits a wide range of physical properties which make it a candidate for photo cells, laser diodes, p-n junction devices and Thin Film Transistor (TFT) displays amongst other industrial applications. As defects create strain and strain influences physical properties which enable these applications, studies of strain are inherently very important.

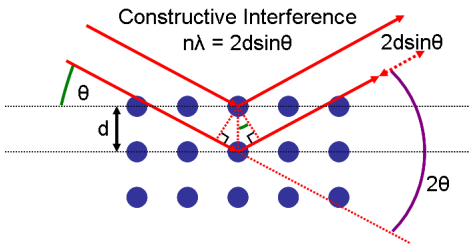

Figure 1: Braggs Scattering Geometry

1.1 Diffraction

Diffraction describes the interaction between a wave and an obstacle.

1.1.1 X-ray Diffraction

X-rays are a type of electromagnetic radiation with wavelengths of the order $1.0\mathring{A}$ and they were discovered in 1895 by Wilhelm Conrad Röntgen [10]. Since then they have been utilised in many fields including; crystallography, radiography, astronomy and material science. Specifically, their application in crystallography has led to the atomic scale study of bulk and surface structures of a wide range of materials by probing the electron density. When an incident plane wave of x-rays is elastically scattered from the electrons in the material a spherical wave results. The interference between spherical waves is observed as fringes understood by the Bragg Law:

$$n\lambda = 2dsin\theta \tag{1}$$

The angles θ at which constructive interference is observed between spherical waves scattered from different atomic planes can be used to calculate the interatomic plane spacing d of the material. Integer n defines the order of the interference fringe. Each Bragg reflection provides information about different planes within the crystal in a single dimension, the observation of several Bragg peaks leads to the comprehension of the atomic structure of the material in 3-dimensions.

An inherent problem for x-ray diffraction is the spatial coherence of the incident beam of x-rays. Resulting diffraction patterns represent an averaging over the illuminated volume of the sample, hence small scale local structures are averaged out. Whereas when coherently illuminated an interference pattern results which is sensitive to local structures.

1.1.2 Coherent X-ray Diffraction Imaging

CXD imaging is applicable when a finite crystal is completely illuminated by a coherent beam of x-rays; a coherent beam is achieved when all scatterers (electrons) within the crystal see the source with the same relative phase. In the Kinematical limit scattering from the whole volume of the nanocrystal will interfere at the detector, therefore the intensity (I(Q)) surrounding each Bragg peak represents the shape of the electron density and is given by

$$I(Q) = |\int \rho(r) e^{i\phi}|^2 \tag{2}$$

where ϕ = Q.r, Q = k_i-k_f and is the momentum transfer local to the bragg peak, k_i and k_f are the incident and scattered wave vectors (where λ is the wavelength, $|k_i| = 2\pi/\lambda = |k_f|$), $\rho(r)$ is the electron number density of the sample and ϕ is a phase factor which represents a displacement of the electron density along the direction of Q. If the reciprocal space amplitude (A) and phase (ϕ) could be measured experimentally, an Inverse Fourier Transform (IFT) could be used to obtain the diffracting electron density distribution. The diffraction signal is detected as photons, the resulting intensity measurement (square modulus of $\rho(r)$ in equation (2) destroys all phase (ϕ) information in reciprocal space; the inherent 'Phase Problem' of X-ray Crystallography. The solution is to sufficiently sample a bandwidth limited intensity measurement akin to diffraction from a finite crystal and solve the phase problem using iterative algorithm methods. Iterative methods use algorithms with constraints built from *a priori* information of the diffracting object and converge to find the lost phase information.

If the crystal was truly real (i.e a perfect lattice), the dependence of the intensity on the FT of the shape function would produce a locally symmetric diffraction pattern about each Bragg peak. In reality crystals have defects, which lead to atomic displacements away from the lattice positions. The resulting change in shape function can be described by the phase factor (ϕ) in direct space which propagates as asymmetry in the observed diffraction patterns. Thus the technique is potentially sensitive to all crystal defects which result in atomic displacements and the derivative of this displacement can be sought to describe a component of the strain tensor.

$$\varepsilon_{ij} = \left(\frac{\partial u_i}{\partial x_j} + \frac{\partial u_j}{\partial x_i} \right) \tag{3}$$

where u represents the displacement field of the objects configuration, the difference between the objects current configuration and its natural state.

1.1.3 Coherence

For the coherent illumination of a finite crystal the incident x-ray beam must be sufficiently coherent in all dimensions. This defines a 3-dimensional region of space within which all scatterers see the source with the same relative phase (coherence volume) and is dependent on the reliability of the x-ray source to produce a coherent beam and the focusing optics required to get the beam to the sample. Until recently the reliability of the source was the predominant factor, hence third generation synchrotron source facilities have made this technique possible.

The coherence length of a beam of light is split into two components, the transverse and longitudinal (temporal) coherence lengths (ξ_T and ξ_L respectively). The transverse coherence is dependent on the source itself and is split into two components the horizontal and vertical. A synchrotron source consists of incoherent emitters confined to a space size d. Two points within the sample will see the source with the same relative phase up to a separation distance ξ_T,

$$\xi_T = \frac{\lambda D}{2d} \tag{4}$$

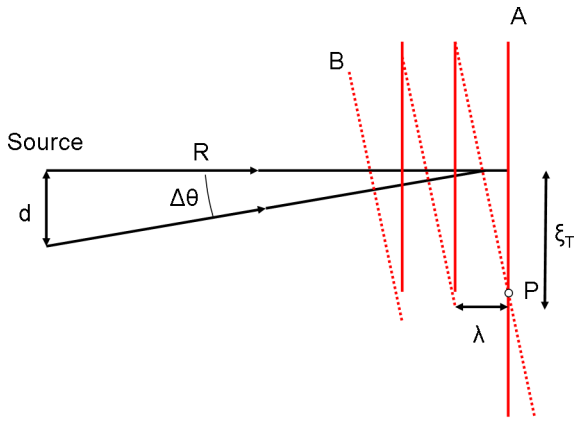

Figure 2: ξ_T described by the interference between two waves propagating from a source size d at point P, adaptation of figure from [11]

where D is the distance from the source to the sample. This is demonstrated in Figure 2; two waves (A and B) of equal wavelength and different propagation directions coincide at the point P. The propagation direction is dependent on the source size, two points at the extents of the source will have the largest divergence angle and set the limit on ξ_T. ξ_T is the distance traveled along the wavefront A from point P in both directions at which destructive interference occurs [11, 12].

ξ_L is dependent on the bandwidth of the monochromator ($\frac{\Delta\lambda}{\lambda}$) attributed to the thickness of the monochromator crystal via the Darwin width. It is coupled to the Optical Path Length Difference (OPLD) of scattering rays through the sample and can be described by the equation,

$$\xi_L = \frac{\lambda^2}{2\Delta\lambda} \tag{5}$$

This is demonstrated in Figure 3; two waves of wavelengths *lambda* and $\lambda + \Delta\lambda$ propagate in the same direction from point A and destructively interfere (π out of phase) at point B, at a distance ξ_L. When the OPLD is smaller than ξ_L the sample is said to be coherently illuminated and meets the required conditions for CXD measurements. For a typical synchrotron source; $\xi_{T-horizontal} = 10\mu$m ,$\xi_{T-vertical} = 50\mu\text{m} > \xi_L = 0.7\mu$m therefore the longitudinal coherence length is the limiting factor for successful CXD measurements. The coherence lengths are large enough to investigate micro/nanosized objects with nanometer precision.

1.1.4 Degree of Coherence

As CXD is reliant on the coherence properties of the incident x-ray beam in 3D it is important to understand how coherent the beam actually is, this cannot be measured directly but can be estimated from the diffraction patterns. The

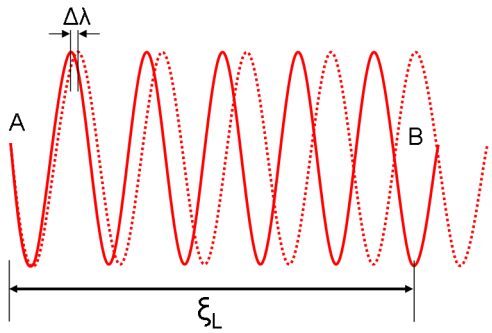

Figure 3: Interference between two waves with different wavelengths $\Delta\lambda$ propagating from the same point A are out of phase at point B a distance ξ_L from the source, figure adapted from [11]

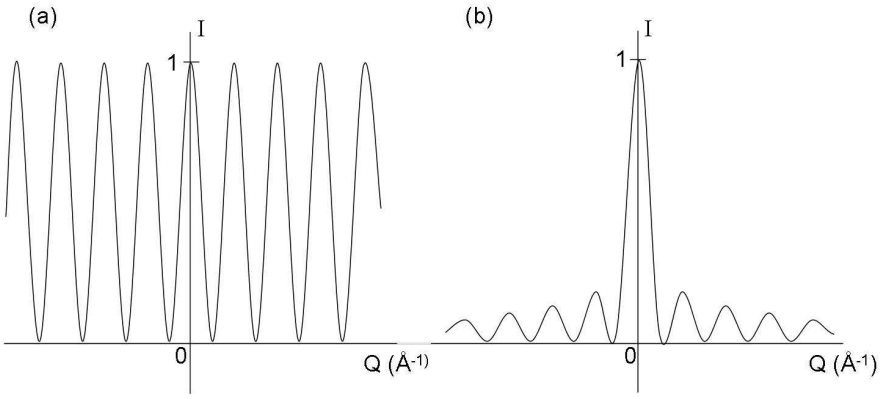

Figure 4: Scattered x-ray interference pattern for (a) two point scatters and (b) all the scatterers inbetween the two points

degree of coherence in its simplest form is a measure of the normalized correlation between two electromagnetic fields; zero being completely incoherent, and where the two fields are effectively identical, equal to one. If in fact they were identical x-rays scattering from two points, the interference pattern that would result is a cosine function, *figure 4(a)*. The fringe spacing corresponds to the distance d between the scatterers through $\frac{\lambda D}{d}$, where D is the distance from the scatterer to the detector. The degree of coherence between the two scattered x-rays can be measured directly by the visibility (V); defined as the contrast of the fringe intensity maxima (I_{max}) and minima (I_{min}) of the interference pattern,

$$V = \frac{I_{max} - I_{min}}{I_{max} + I_{min}} \tag{6}$$

For the coherent illumination of two point scatterers the visibility of the interference pattern would be equal to 1 for all fringes, and drop to zero as the two fields are varied to the state where they are π out of phase.

So far we have considered two point scatterers, practically a finite crystal consists of many scatterers the case where the two scatters lie on two facets of a finite crystal and all of the scatterers inbetween contribute, a 1D slit function results *figure 4(b)*. Therefore the fringe spacing determines the size of the crystal facet to facet in the corresponding direction. Equation 6 is still valid and in the presence of perfect coherent illumination a visibility of one is expected.

1.1.5 Optics

The optics on a beamline required to maintain a coherence volume large enough to analyse crystals using CXD has been realised in the last 10 years [13]. Physically getting the beam from the source to the sample is experimentally challenging, optical components must handle heat load, vacuum environment and be stable to maintain ξ_L (the limiting coherence property). Improvements in the quality of monochromator crystals have improved the longitudinal coherence length set by equation 5. Longer longitudinal coherence lengths can be achieved but the x-ray photon flux is compromised as a result. In order to look at smaller and smaller crystals more flux is required as there is less sample volume to scatter from. In addition to coherent beams third generation synchrotron sources provide enough intensity to obtain sufficient statistics for CXD measurements from finite nanocrystals. The flux is spread across a relatively wide beam (several hundred microns) and for sub micron crystals leads to the introduction of focusing optics. Common choices include Fresnel Zone Plates, Kirkpatrick-Baez (KB) mirrors and compound refractive lenses. Their use is dependent on the size of the focus and intensity required. Robinson et al. [14] discuss the advantages and disadvantages of each method concluding KB mirrors are the most suitable for finite nanocrystal CXD for optimization of both flux and coherence. The introduction of more optics has a significant impact on the coherence properties of the incident beam, traditionally in a CXD beamline as fewer components are used as possible to maintain the coherence properties of the incident beam.

1.2 Phase Retrieval

An iterative mathematical approach is employed to solve the 'Phase problem' and the origin of the name 'lensless imaging'; moving from direct space to reciprocal space and back again, *a priori* information about the crystal is used to constrain each iteration until a set of amplitudes and phases is found to represent the measured intensity around a Bragg peak. The successful retrieval of phase for a measured diffraction pattern is dependent on overcoming several hurdles; sampling the diffraction pattern sufficiently to retrieve all the information in the signal and the broader problem of finding unique solutions and identifying ambiguous solutions.

1.2.1 Oversampling

The ability of the phase retrieval method to find a solution depends on the sampling ratio; the rate at which the intensity is sampled. A signal or function is bandwidth limited if it contains no energy at frequencies higher than a defined bandwidth. Hence, it is constrained in terms of how rapidly it changes in time, and consequently how much detail it can convey inbetween discrete instances of time. The sampling theorem states that uniformly spaced discrete samples are a complete representation of the signal if this bandwidth is less than half the sampling rate. For example, a signal with a maximum frequency f_{max} needs to be sampled at a frequency of at least $2f_{max}$, the Nyquist critical frequency, to be resolved. In the case of x-ray diffraction measurements Sayre [15] observed that if the square modulus of the signal is measured, the intensity from equation 2, the sampling rate required is oversampled by a factor of two, i.e ($4f_{max}$). The oversampling ratio is defined in direct space in each dimension as

$$\sigma = \frac{ArraySize}{CrystalSize} \tag{7}$$

where the crystal size can be estimated by the size of the Support; the defined region of direct space within which the crystal can exist.

It is important to note the oversampling requirement is controversial in 3-dimensional problems; Miao et al. findings [4] suggest the limit does not apply to each dimension individually but the whole volume measured to less than one half the total volume measured. Millane suggests [16] σ=2 in each dimensions and the corresponding support $1/2^3(1/8^{th})$ the total volume measured.

The phenomenon of 'Aliasing' arises when discretely sampling a continuous function that is not bandwidth limited to less than the Nyquist critical frequency. In this case all of the power spectral density that lies outside of the frequency range ($-f_c<f<f_c$) is spuriously moved into that range and would be expected in the first case. There are two ways to overcome Aliasing; i) sample at a sufficient rate to obtain four points per period of the highest frequency present, ii) identify the natural bandwidth of the signal or else enforce a known limit by analog filtering of the continuous signal before it is sampled.

With this in mind, all data is measured with an oversampling ratio of approximately 3 to ensure the data can be solved mathematically.

1.2.2 Uniqueness

The discrete nature of the measurement leads to ambiguous solutions. A problem with N knowns (amplitudes) and N unknowns (phases) potentially has many solutions, the application of *a priori* knowledge provides sufficient constraints for the algorithms to identify the correct solution. This is not always satisfied. One can envisage a solution space whereby once an algorithm finds a local minima it remains there as the changes imposed upon it based on the defined constraints cannot change it enough to find an alternate solution. At present distinguishing between the local minima and the global minima (the actual solution) is difficult and is dependent on the phase retrieval algorithms discussed in Section 1.3. Once overcome the problem of multiple ambiguous solutions of a direct space function (*f(x)*) remains, whereby rather than finding a single solution, a set of direct space solutions are obtained where the Fourier Moduli are identical:

Twinning - *f*(-x)* the complex conjugate of the electron density.

Position - $f(x+x_0)$ a shift in the position of the diffracting object.

Factorisability - $e^{i\phi}f(x)$ a phase factor applicable to the entire function and is necessary for multiple ambiguous solutions to exist [17].

There are several solutions presented in the literature for overcoming the uniqueness problem and the existence of ambiguities will be discussed after the algorithms have been introduced.

1.3 Phase Retrieval Algorithms

Each algorithm works with different constraints, with certain algorithms being suited to particular problems. The algorithms used thus far include:

1. Gerchberg-Saxton Algorithm [18]
2. Error-Reduction (ER) Algorithm [19]
3. Hybrid Input Output (HIO) Algorithm [6, 19]
4. Variations on (1-3) and Alternate algorithms [20]

1.3.1 Gerchberg-Saxton Algorithm

The motivation of Gerchberg and Saxton (GS) was to find a method whereby the phase of a wavefunction may be recovered from simultaneous measurements in the image and diffraction planes [18]. As the amplitudes in these planes are related by Fourier Transform (FT), a coherent illuminating wave is required. It was proposed a similar method could be used in X-ray crystallography, however the technical difficulties involved in making an X-ray measurement in the image plane limited its application to electron microscopy.

In the GS algorithm there are two known constraints:

1. Magnitude of the amplitudes in the image plane.
2. Magnitude of the amplitudes in the diffraction plane.

The algorithm operation is represented in the flow diagram in Figure 5, the algorithm iterates between direct and reciprocal space using the amplitudes in each space as the constraint for estimating the unknown phases from a random starting position. The feedback loop is instigated by a measure of the quality of the result.

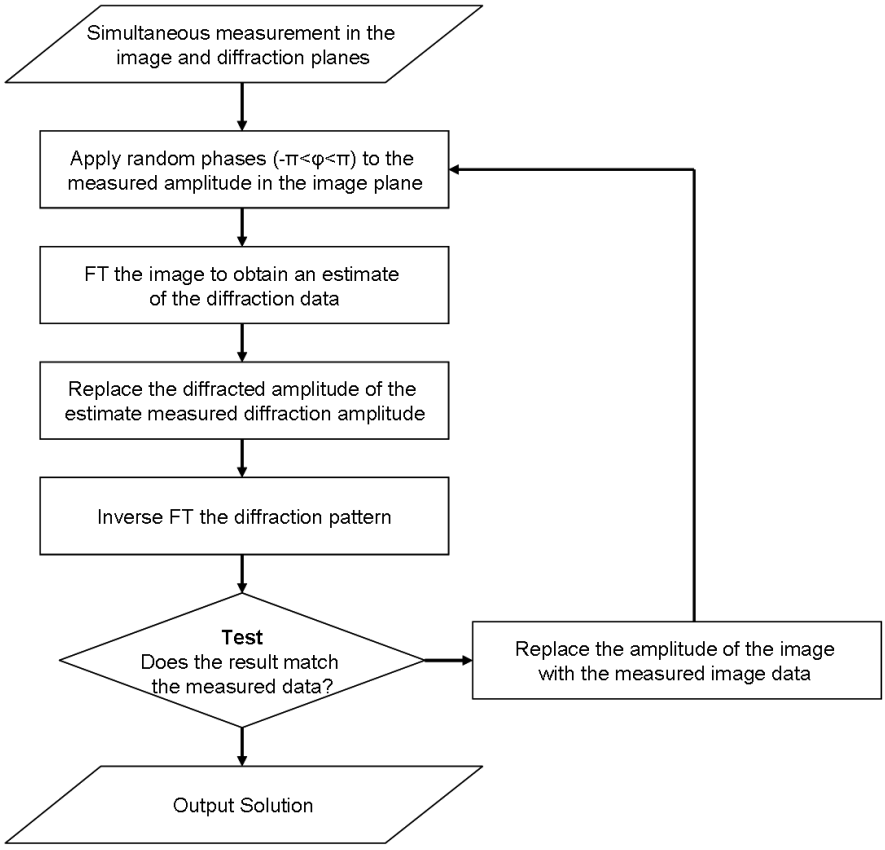

Figure 5: Flowchart of the Gerchberg Saxton(GS) algorithm operation

How does one test the quality of a result?
The simple observation of the FT of the result compared to the experimental provides a qualitative measure. Quantitatively an error metric χ^2 is defined as the normalised squared difference between the reconstructed (A_{alg}) and measured amplitudes (A_{exp}) in reciprocal space.

$$\chi^2 = \frac{\sum |A_{alg}|^2 - |A_{exp}|^2}{\sum |A_{exp}|^2} \tag{8}$$

Hence when the direct space reconstructed amplitudes matches the experimental amplitudes $\chi^2 = 0$ the problem is solved.

1.3.2 Error-Reduction (ER) Algorithm

Fienup suggested an extension to the GS algorithm in 1978 [19] whereby the intensity measurement is only made in reciprocal space. He proposed to use real-space constraints in place of the real-space intensity measurement. The most common constraints being:

1. Positivity - The real-space density should not be negative, which in the case of a perfect single crystal is physically expected.

2. Finite support - The real-space density occupies a confined region within the volume of real-space measured by the diffraction data.

Initially it was thought that both constraints were required, however Fienup later showed [6] using a sufficiently tight support constraint the complex problem is no harder. Allied to the original GS algorithm (*Section 1.3.1*), the reciprocal-space constraint is the measured diffraction data and the algorithm operation is shown in Figure 6.

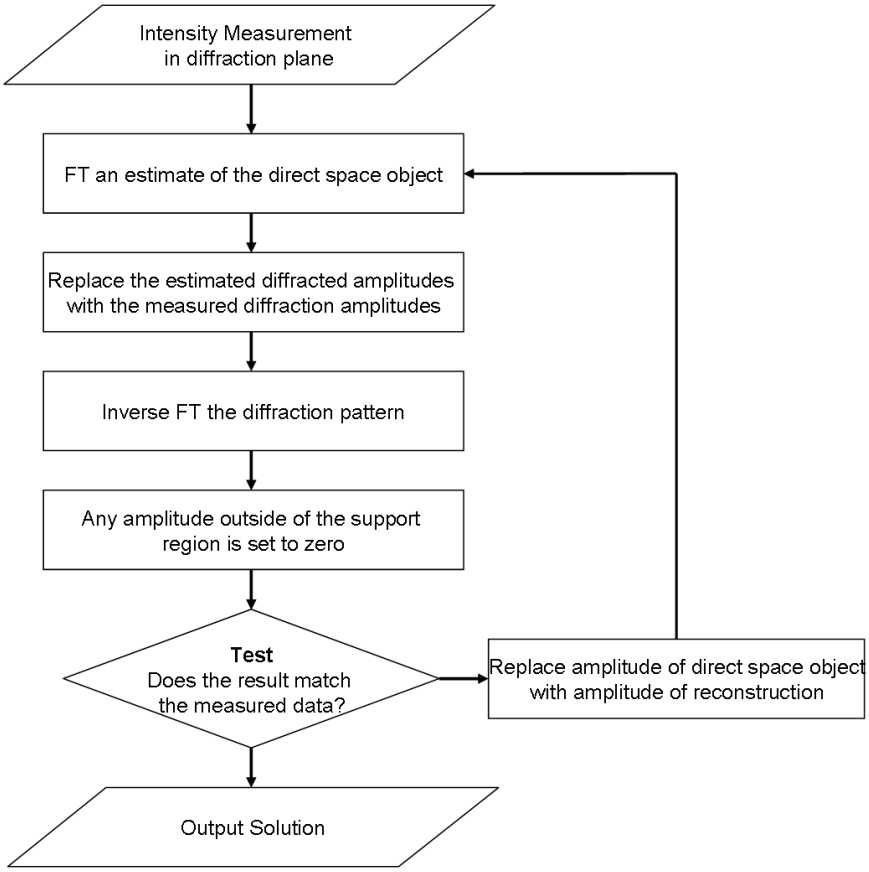

Figure 6: Flowchart of the ER algorithm operation

FT an estimate of the real space density $f_k(x)$ to obtain $F_k(q)$, often a copy of the chosen support as the solution is expected to be of this order. Replace the

magnitude of the reconstructed diffracted amplitude by the measured diffraction amplitudes $F'_k(q)$. IFT the result and apply the constraint set by equation 9;

$$f_{k+1}(x) = \begin{cases} f'_k(x) & \text{if x} \in S \\ 0 & \text{if x} \notin S \end{cases} \tag{9}$$

here, any amplitude or phase outside of the support region (S) is set to zero, as physically it cannot exist, the result is an estimate for the real space density $f_{k+1}(x)$. Test the quality of the reconstruction and repeat the process until a solution is found.

The ER algorithm itself converges very slowly, once all of the amplitudes and phases lie within the support the algorithm will stagnate. The algorithm has no way of distinguishing between all solutions which contain phases and amplitude within the support, highlighting the problem of finding a unique solution in this case.

1.3.3 Hybrid Input Output (HIO) Algorithm

The slow convergence and stagnation tendency of the ER algorithm has led to the formulation of alternate algorithms. One class of these is the Input Output algorithms, developed by Fienup [19]; here the basic process of ER is maintained but the constraints are different, the input is no longer the current best estimate of the dataset, it is in fact the driving function for the next output (derived from a combination of the current and previous iteration). This produces a large amount of variation in the following input, aiding the algorithm to avoid stagnation although it remains susceptible to it.

The constraint again applies outside the support; the reconstructed solution $f\prime_k(x)$ is used to alter the driving function $f_k(x)$ by a factor β.

$$f_{k+1}(x) = \begin{cases} f\prime_k(x) & \text{if x} \in \text{S} \\ f_k(x) - \beta f\prime_k(x) & \text{if x} \notin \text{S} \end{cases} \tag{10}$$

It is clear that as β approaches unity, the algorithms operation approaches the ER algorithms regime; as χ^2 drops the previous iterate begins to replicate the current solution, hence those amplitudes and phases outside of the support will be set to zero, *see Equation 9*. Beyond a value of 1, amplitudes and phases outside of the support will oscillate between positive and negative values forcing the algorithm further away from a solution. β values in the range 0.8-0.95 are common, any lower and the changes made are insufficient to move out of local minima in solution space and stagnation results.

1.3.4 Alternate Algorithms

To date several variations on the existing ER and HIO algorithms have been used as iterative approaches to the phase problem: they include phase constrained HIO and ER [21], Millanes HIO [22], guided HIO (gHIO) [23] and Solvent Flipping (SF) [24]. There are also alternative algorithms which include Difference Map (DM) [25], Averaged Successive Reflections (ASR) [26], Hybrid Projection Reflection (HPR) [27] and Relaxed Averaged Alternating Reflectors (RAAR) algorithm [28].

These algorithms are discussed fully by Marchesini [20] and he concludes HIO is the most effective algorithm at finding a solution and gradient based methods such as ER or SF can be used to polish up the solution, similar observation with 3D datasets are shown in *Section 3.5*. The basis for phasing in this work is built on that developed by Robinson et al. [1–3] and uses Fienups HIO and ER with additional phase constraints dubbed Phase Constrained HIO (PC-HIO) introduced by Ross Harder [21] and Phase Only ER (POER).

Phase Constrained HIO sets maximum and minimum thresholds for the phase that the algorithm can assign in direct space. The method is often applied to crystals with very small phase variations and improves the algorithms ability to find the correct unique reconstruction. Additionally it prevents the formation of vortices as the phase is not allowed to form a 2π phase wrap.

Phase Only ER is the ER algorithm with an additional constraint; amplitude can exist outside the support region if its phase is zero. Practically this amplitude manifests as noise in the data and has proven advantageous in refining reconstructions

1.3.5 Algorithm Extensions

Inability to converge and solution uniqueness/ambiguity are the key problems faced by the phase retrieval algorithms. Fienup and Wackerman [29] observed from multiple starting points stripes were found to be prevalent in 2D reconstructions; different random starting points resulted in different orientations and frequencies of stripes. Originating from phase singularities (vortices) in reciprocal space, vortices present, in pairs, centrosymmetrically in the image and with opposite phase wrapping, of total 2πn. Two methods; the 'voting method' and the 'patching method' are discussed, in the voting method three random reconstructions are made, of the two that correlate the most an average/combination is taken and used to drive the next fit. The patching method is an extension of the voting method, the stripes extend beyond the support and are used to locate the vortices and subsequently patch them out. In 3D vortices present as loops which are much rarer than 2D cases [2], the proposed solution is to reduce the background to prevent the algorithm assigning phase values large enough for vortices to form. A valid approach that neglects the scenario whereby large phase variations in a crystal are expected, distinguishing between an anomalous vortex and physical phase wrap in this case becomes problematic.

Guided HIO has been developed by Chen et al. [23] and builds on the principle of maintaining features from multiple solutions. Running the phasing algorithm through x number of random starting points, the best dataset is sought and combined individually with all of the other solutions, these solutions then drive the next generation of solutions; the process is then repeated until the algorithm converges. A version of this algorithm was written for the Bragg scattering geometry, conclusions drawn were:

1. The algorithm always tends towards the initial solution and suffers similar stagnation problems as HIO and ER methods.

2. A useful method for the determination of ambiguous solutions via cross correlation, discussed further in Section 3.4.4.

Marchesini et al. [30] developed an algorithm for which no *a priori* knowledge is required, the support is built from the autocorrelation of the data and

tightened until the algorithm converges. Briefly, a gaussian is convolved in each dimension with the reconstructed object. This slowly reduce the size of the support used to constrain the result until it converges to the correct solution. It has to overcome the autocorrelation function as a potential solution and must converge when the solution has been found, if the support encroaches on the reconstruction an incorrect solution will result.

1.4 Examples of Successful Phase Retrieval

Several examples of successful phase retrieval methods have been reported to date and will be discussed.

The first reconstruction from a 2D diffraction pattern was demonstrated by Miao *et al.* [31] with a non-crystalline test object at 75nm resolution. Later Robinson *et al.* [32] used CXD around a $11\bar{1}$ Bragg peak to recover the shape of an Au nanocrystal. This was soon followed by the successful recovery of a 3D test object [33] and a 3D Au nanocrystal by Williams *et al.* [32, 34, 35] at 50nm resolution. Since then a large number of test objects and samples have been successfully recovered from both x-ray [36–40] and electron [41, 42] diffraction data. Those most relevant to CXD of nanocrystals are detailed. Favre-Nicolin *et al.* [43] reconstructed the shape of a single Silicon (100nm diameter) nanowire with 15nm resolution and discussed the effects of the beam interacting with the sample, the observation of wires 'breaking' whilst in the beam implies radiation damage is a serious limitation. Chamard *et al.* [44] identified via simulation the reciprocal space features exhibited by nanowires with stacking faults. Minkevich *et al.* [45] have studied arrays of silicon lines and concluded by inspection with finite element models the origins of reciprocal space features attributed to large internal strains. Reconstruction of individual Au nanocrystals (sub 100nm) has been achieved by Schroer *et al.* [46] at 5nm resolution; obtaining sufficient intensity from a small object to reconstruct it by nanofocussing with a Zone Plate and maintaining a coherent beam. As focussing optics improve, resolution improves and the illuminating beam size drops. So far only the recovery of finite objects has been discussed but it is possible to measure extended objects using a combination of CXD and microscopy methods called 'ptychography' [47–49]. The basis for this method is measuring multiple diffraction patterns from overlapping regions on a sample, the subsequent overlap provides a constraint strong enough to reconstruct the illuminated region of the sample.

Alternative applications of coherent diffraction methods include; Biological imaging, Shapiro *et al.* [50] used soft x-ray diffraction microscopy to image yeast cells to 30nm resolution; and Direct Holographic Inversion [51], which overcomes the central problem of phase retrieval by using a nanoscale reference aperture close to the sample which phases the interference pattern. In this case iterative algorithms like those discussed in *section* 1.3, can be used to further enhance the spatial resolution of the image. The CXD technique is also a strong candidate for future X-ray Free-Electron Lasers (XFELs), high intensity coherent pulses of femtosecond duration allow single shot imaging.

1.5 X-ray Free Electron Laser sources

A Free Electron Laser (FEL) is a laser that shares the same optical properties as conventional lasers. Emitting a beam consisting of coherent electromagnetic

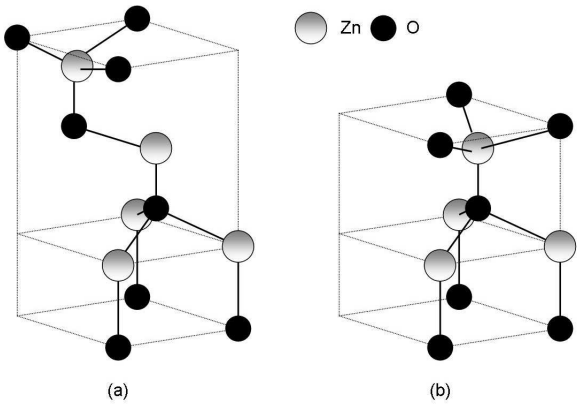

Figure 7: Unit cell of (a) zincblende ZnO (b) wurtzite ZnO

radiation capable of reaching high power. The European XFEL[1] expects to produce a brilliance billions times stronger than third generation synchrotron at its brightest intensity and 10^4 times brighter on average across the whole beam. Its operation is very different compared to gas, liquid or solid-state lasers, which rely on bound atomic or molecular states, the 'free electron' term arises from the use of a relativistic electron beam as the lasing medium. This gives them the widest frequency range of any laser type, and makes many of them widely tunable, currently ranging in wavelength from infrared ISIR, Osaka University, through to soft X-rays at the FLASH facility, at the Deutsches Elektronen-Synchrotron (DESY) in Hamburg. The potential of FEL sources for CXD has already been shown by Chapman *et al.*; initially in the reconstruction of a test object [52] and later x-ray holography of polystyrene spheres as they are vaporised by the incident beam [53]. The proposed European XFEL will produce pulses of less than 100 femtoseconds providing the time resolution to probe chemical and physical processes with precision yet to be achieved by other characterization methods. The speed at which the measurements are taken is problematic itself and there are many engineering hurdles to overcome, but the potential in the fields of CXD and Holography are clear [54].

1.6 Zinc Oxide

Zinc Oxide is a unique material; a transparent semiconductor with a direct band gap of 3.37eV and a large exciton binding energy (60meV), it exhibits piezoelectric [55]and pyroelectric behaviour. ZnO exists in the stable wurtzite phase and the metastable zincblende phase, *figure 7*. Nanoscale synthesis has produced a large variety of morphologies with potential applications in optoelectronics, sensors, transducers and life-sciences. Current industrial applications range from catalysis in the vulcanization of rubber to sun screen as it absorbs ultraviolet

[1] http://xfelinfo.desy.de/en/start/2/index.html

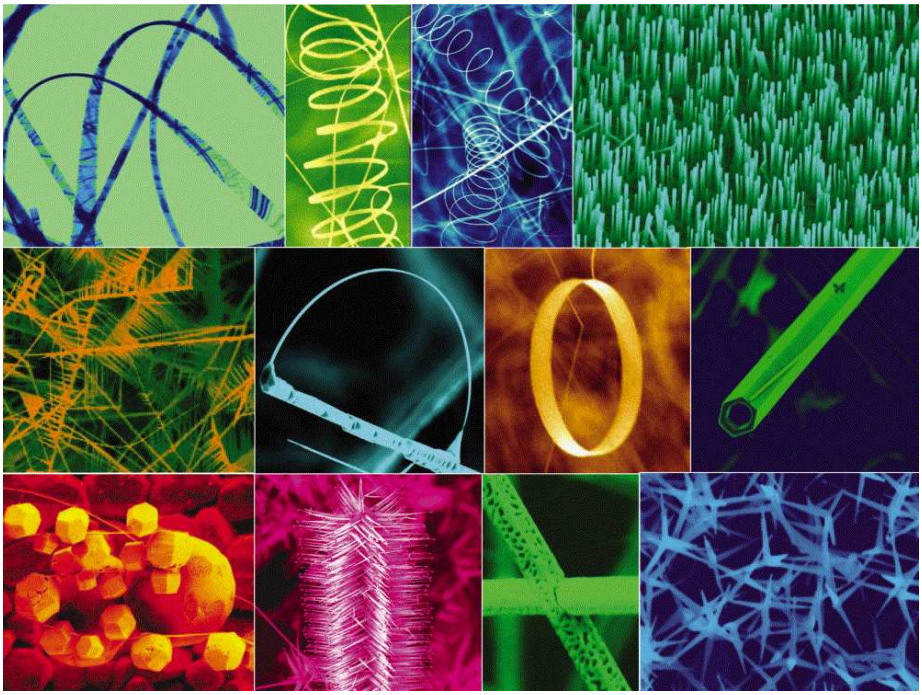

Figure 8: Variation in ZnO nanostructures grown by Wang *et al.* [57]

light. ZnO is also environmentally safe and relatively cheap compared to Gallium Nitride (GaN) material that demonstrate similar physical attributes and is used widely in electronics applications.

Such a popular material demands attention and the literature regarding ZnO is vast. Z. Wang provides a comprehensive overview of the growth methods, properties and corresponding applications of ZnO nanomaterials [56] along with detailed discussion of the variation in nanostructures synthesised [57]. Synthesis methods include; Chemical Vapour Transport Deposition (CVTD), Metal-Organic Chemical Vapour Deposition (MOCVD) and solvent based methods. Focus will be placed on the CVTD method [8, 58] which can be tuned to produce nanorods, nanowires, platelets and tetrapods; nanoscale branched structures, demonstrated with SEM[2] in Figure 11 and Figure 8 highlights some more exotic nanostructures of ZnO grown by Wang *et al.* [57].

The tetrapod structure in *Figure 11*, is of specific interest as it has been proven via TEM [59] to possess both known phases of ZnO, wurtzite arms and a zinc blende core [60]. The main advantage of using CXD to investigate tetrapods is that different structures and crystal orientations produce different Bragg peaks which can be measured independently. This would allow the independent measurement of each side of an interface, in this case the Zinc blende core and the four wurtzite arms, *see Figure 9*. The experimental sample manipulation procedure at present is not accurate enough to map several Bragg

[2]Carl Zeiss XB1540 "Cross Beam" focussed-ion-beam microscope at London Centre for Nanotechnology, specification: http://www.london-nano.com/content/lcnfacilities/crossbeam

peaks from a single crystal, if the orientation of two crystals at a single interface is known and the experimental accuracy improved the experiment is feasible. Tetrapods have been fabricated into Schottky diodes by Newton et al. [58, 60] using a Focused Ion Beam (FIB) to connect a single tetrapod to contacts on a substrate.

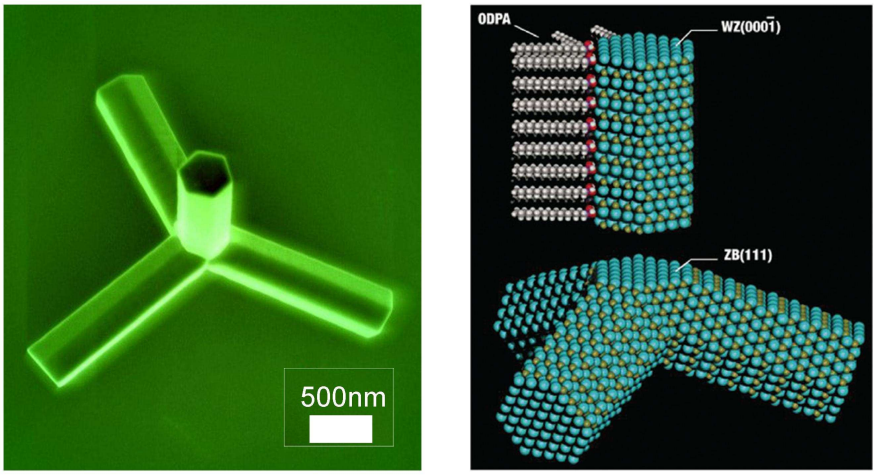

Figure 9: ZnO Tetrapod (a) produced via CVT on Silicon (100) substrate imaged with Scanning Electron Microscopy (SEM) (b) predicted structure [61]

Nanorods are also of interest for similar applications, an overview of their growth, properties and applications is given by Yi *et al.* [62]. Highlights of the work to date include; the fabrication of a Schottky diode with a single ZnO nanorod by Heo *et al.*, Liao *et al.* [63] demonstrated the diameter of nanorods will affect the properties of a gas sensing device; those rods with smaller diameters possessed larger compressive stress and increased surface defects, thus made them more sensitive to oxygen adsorption. The first single nanowire ZnO Light Emitting Diode (LED) was demonstrated by Bao *et al.* [64] and exhibits broad sub-bandgap emission at room temperature; an LED consists of a p-n junction; p-type conductors have an abundance of positive charge carrying holes and n-type have an abundance of charge carrying electrons (p-type silicon and n-type ZnO in Baos' case). Electron-abundant n-type ZnO nanocrystals are common, missing oxygen atoms within the regular ZnO crystal structure create relative overabundances of zinc atoms and give the semiconductors their n-type, conductive properties. The necessity of a dopant for p-type conduction was implemented by Xiang *et al.* [65] in the synthesis of the first p-type nanowires. It is expected to pave the way for pure ZnO LEDs, transistors, spintronics and Dilute Magnetic Semiconductors (DMS).

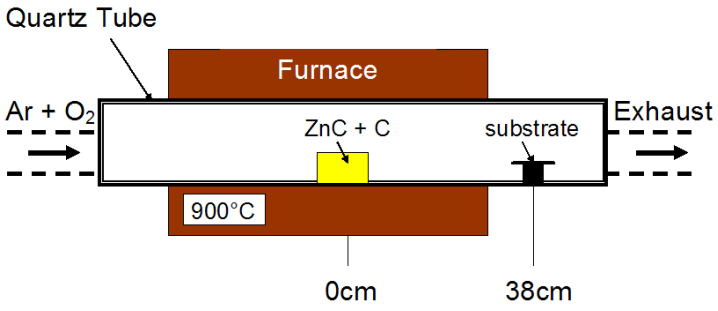

Figure 10: Schematic of ZnO furnace arrangement

2 Methods

2.1 ZnO

2.1.1 Nanocrystal Synthesis

Zinc oxide nanocrystals were produced using the aforementioned CVTD method. It is generally agreed the growth mechanism is either vapour-solid [66] or vapour-liquid-solid [67] depending on the growth parameters and the reaction proceeds via the carbothermal reduction of zinc carbonate, $ZnCO_3$.

$$ZnCO_3 \longrightarrow ZnO + CO_2 \tag{11}$$

$$ZnO + C(CO) \longrightarrow ZnO_x + CO_2 \tag{12}$$

The carbon within the mixture promotes a deoxidation reaction, the resulting sub oxides of ZnO nucleate and oxidise to form nanocrystals. For the large scale fabrication of nanoscale devices the growth needs to be controlled; the nucleation of several different ZnO morphologies has been successfully controlled using closely matching substrates, such as sapphire c-plane (Al_2O_3 and GaN). Catalysts have been used to seed both nanowire (Au [68] and Sn [69]) and nanobelt growth (Au and Indium [68]); the type of catalyst can affect morphology and crystallite size. If the shape of the catalyst can be controlled does the subsequent ZnO structure change and affect the crystal properties?

The schematic in Figure 10 details the experimental setup for this method. A mixture of zinc carbonate and graphite powder; weight ratios of (5:1) and (10:1) were placed in a silica boat in the centre of a quartz tube surrounded by a furnace. Argon carrier gas was introduced at a flow rate of 500-700 Standard Cubic Centimetres per Minute (sccm) with oxygen composition in the range 3%-5%. The furnace was heated to 900°C, the onset of carbothermal reduction produces supersaturated ZnO_x vapour. The subsequent oxidation of this vapour leads to the deposition of a white layer , *see Figure 12(a)*, of material onto a Silicon (111) substrate placed downstream (150°C) parallel to the gas flow. The crystals grown depend on several variables; temperature, pressure within

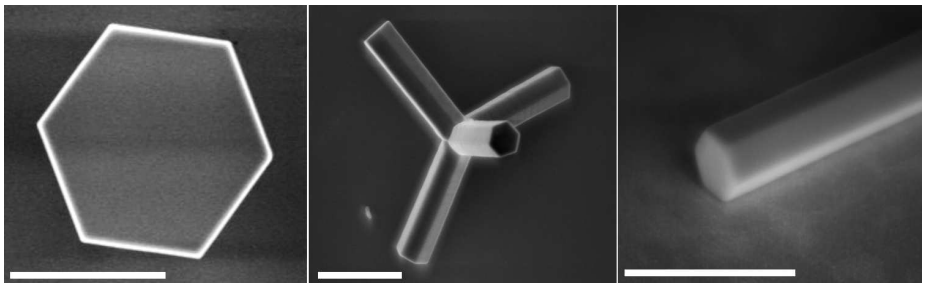

Figure 11: SEM micrographs of a) hexagonal plates b) tetrapods c) nanorod morphologies; Scale Bar = 1μm [58]

the quartz tube, oxygen content, volume of source material, the shape of the source boat and substrates used.

The nanocrystals synthesised by Marcus Newton previous to this project are shown in *Figure 11*, they include hexagonal plates (200nm thick x 1-2μm), nanorods (0.2μm x severalμm) and tetrapods; multiarmed structures joined at a central point surrounded by arms with sometimes tapered hexagonal facets at higher pressures.

It is important to note the furnace system was moved to a new location and the strength of the exhaust severely affected the morphology of the grown nanocrystals. Maintaining atmospheric pressure favoured the rod morphology and tuning of the variables allowed rods of dimensions in the range 0.2-2μm in diameter x 2-5μm in length to be grown. At higher substrate temperatures smaller structures were observed, including nanowires (60nm x 40μm), exhibited in *Figure 27C*.

2.1.2 Sample Preparation

Due to the strong ionising power of the x-ray beam crystals can move when placed in the incident beam. Several methods were tested to adhere the particles to the surface without changing their morphology, they include; (i) evaporate a layer of Titanium (nm) onto the crystals; (ii) fabricate on substrates with matching lattice parameters e.g Si (111) and sapphire c-plane, previously Liang et al. [70] had used glues and paints, these proved to be unstable as they did not fully crystallise; (iii) grow the oxide layer on the substrate to encase the base of the crystals. Growing the oxide layer post synthesis proved the most successful method for adhering samples to the substrate, combined with improvements in the stability of the beamline allowed individual crystals to be analysed for several days. As the oxide layer is grown the substrates colour changes (blue for an additional 80nm of oxide layer), gradients in the oxide layer are avoided by increasing the oxygen flow rate and placing the sample in the hottest region of the furnace where the temperature gradient across the sample is the lowest, *see Figure 26*. It is important to note an interaction between the crystals and the surface is expected.

Initially experiments were carried out in the focussed mode of operation and required small crystals. Subsequent experiments led to an *in-situ* approach which could only operate in unfocused mode, it was necessary to tailor the rods

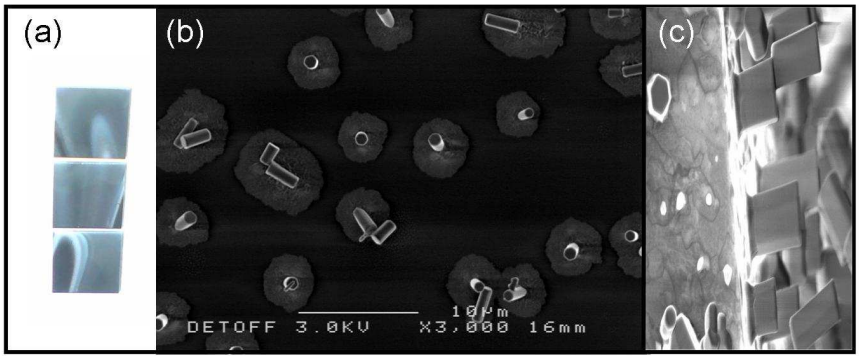

Figure 12: SEM micrographs of a) top view and (b) side view of multiple nanorods on a Si(111) substrate with a post synthesis oxide layer growth

to larger sizes to get enough intensity from the samples.

2.2 Coherent X-Ray Diffraction Imaging

This section will introduce the CXD beamline setup for the different sample dependent operational modes (focussed and unfocussed), the optics required to get the beam to the sample and the data acquisition method.

2.2.1 Beamline Setup

The x-ray beam at the Argonne National Laboratory Advanced Photon Source was used. Beamline 34-ID-C uses a beam splitting mirror to direct the beam onto a silicon (111) double crystal monochromator. The monochromator was used to select 9keV monochromatic x-rays (lamba=1.39$\AA$) with a bandwidth (1eV) small enough to provide a longitudinal coherence length ($\xi_T \simeq 0.7\mu$m) according to equation 5. There are two principle modes of operation defined by the size of the beam required in the transverse direction:

Unfocused setup : the beam is selected using Roller Blade slits, depending on the crystal density on the sample surface the required area of sample illumination can be set comfortably to(20-100μm x 20-100μm).

Focused setup : the beam is again selected using Roller Blade slits (100μm x 100μm) and is focussed using Kirkpatrick-Baez (KB) mirrors to a square approximately 1μm x 1μm, providing a significant increase in intensity compared to the unfocussed approach, thus is favourable for smaller crystals which require a greater photon flux.

Sample stages move the sample into the beam, illuminating all crystals in the beam footprint. The beam footprint on the sample is incident angle dependent; from large angles to grazing incidence the illuminated area on the sample will drop accordingly. The footprint is varied to locate and isolate crystals on the

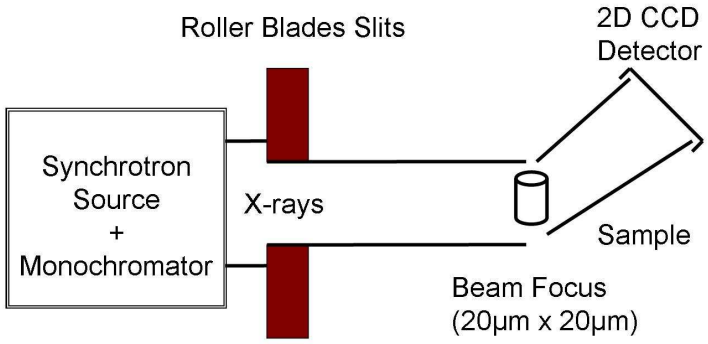

Figure 13: Schematic of unfocused mode of beamline operation

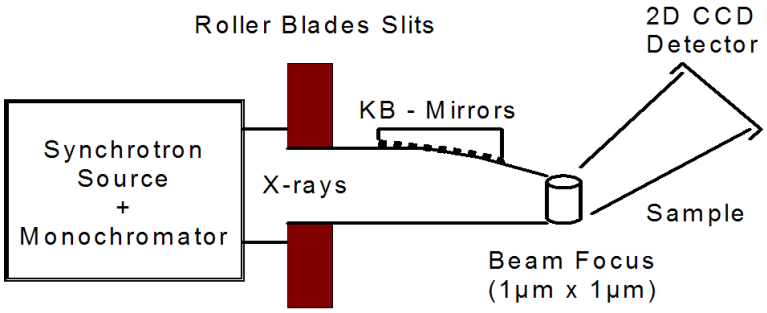

Figure 14: Schematic of focused mode of beamline operation

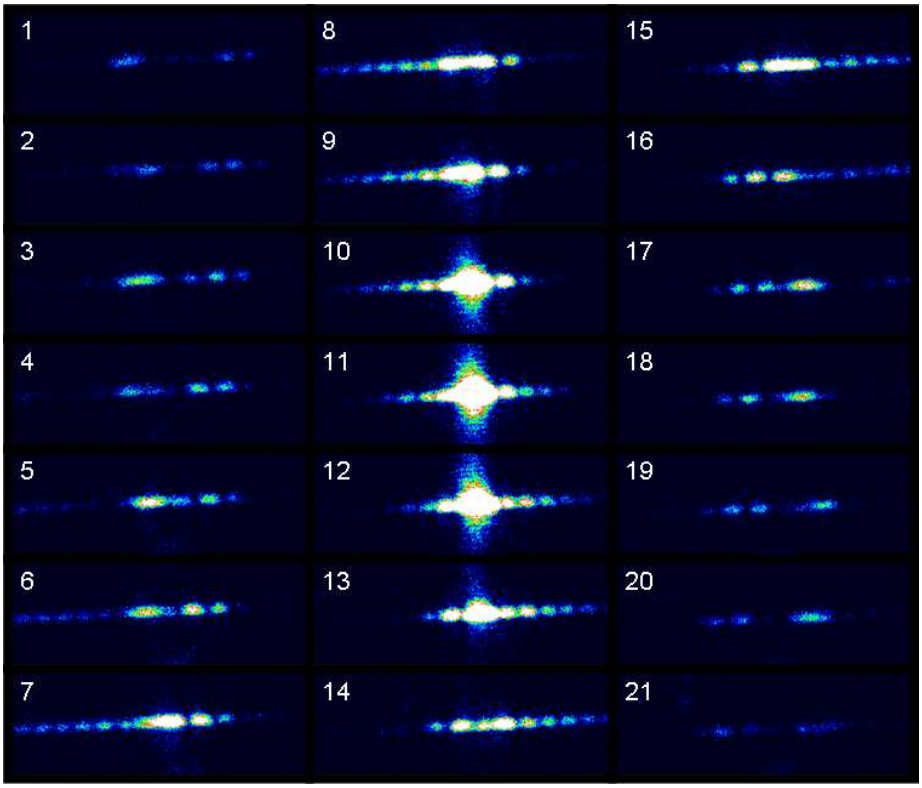

Figure 15: 2D diffraction patterns from a rocking scan of ZnO (101) Bragg peak

surface; for a sample with a low crystal density a large footprint illuminates the few crystals that satisfy Braggs law for that particular orientation. If the sample is densely populated and multiple diffraction peaks from different crystals are being detected the beam size and footprint can be decreased until a single crystal in the required orientation is illuminated.

For ZnO nanorods two orientations are probable, rods stood on end and rods lying on their sides at random rotations relative to the samples surface plane. By choosing a specific orientation of the crystal; in this case a rod stood on end, the Roper Scientific direct-detection CCD is placed 1-3m behind the sample and is moved to the correct Bragg angle for in this case the brightest (101) ZnO reflection. The sample is translated in the beam until a crystal on the sample happens to have the right orientation and adjustments to both the sample position and the detector arm to allow the diffraction pattern to be centred on the detector. The distance to the detector defines the rate at which the data is sampled, governed by the oversampling rule, Section 1.2.1. Through rotation of the sample in the surface plane (θ) rocking curves are taken through the Bragg peak, the diffraction pattern is rocked through the detector and 2-dimensional diffraction patterns, *see Figure*15, are concatenated to produce a 3-dimensional dataset, *see Figure 16*. The cut planes in *Figure 16* highlight the fringes resulting from coherent illumination of a finite single crystal.

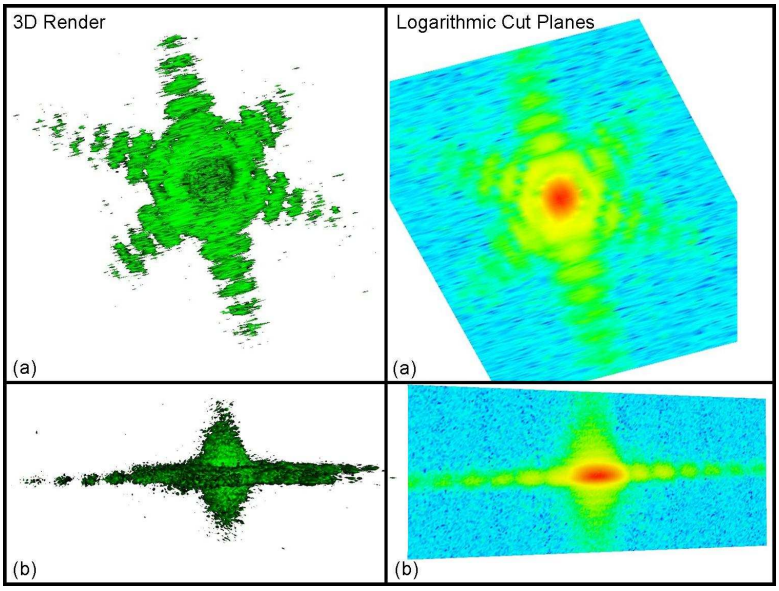

Figure 16: Dataset 27: 3D render of slices in Figure 15 (a) Side (b) Top view and Logarithmic cut planes for corresponding isosurfaces

2.2.2 Experimental Data Treatment

The CCD detector is read off into WinView data acquisition software and output files in SPE format (ASCII text file). Data manipulation and analysis programming capabilities are being constantly improved upon, hence only a brief outline of the current data treatment method will follow.

The SPE files are converted into Sp4Array() format introduced by Williams [2] and Pfeifer [3]. A set of C-program libraries are compiled for use in a python environment using a Simplified Wrapper and Interface Generator (SWIG)[3]. For 3-dimensional visualisation the open source Visualization ToolKit (VTK)[4] was used.

Depending on the amount of oversampling required, the data can be binned accordingly to save time in data processing however this impinges on the resolution of the result. The data must also be centred in the array for the FT to function correctly, the FT is a mathematical translation to reciprocal space units, those points in the centre of the array move to the edge and those at edge move to the centre. Introducing asymmetry at this stage leads to a gradient in the phase of the reconstructed image, this gradient can be used to identify if the data is centred correctly. By observing the autocorrelation function (FT of the measured intensity) of the data as a function of position; the program 'dataCentre-5x5.py' maps the autocorrelation function by removing 2-dimensional slices of data in each dimension through the central point, and does the same operation for shifts in the data's position of ± 2 in each dimension relative to the centre. The ouput of the x-y, x-z and z-y 2D cross sections allows

[3]http://www.swig.org
[4]http://www.vtk.org

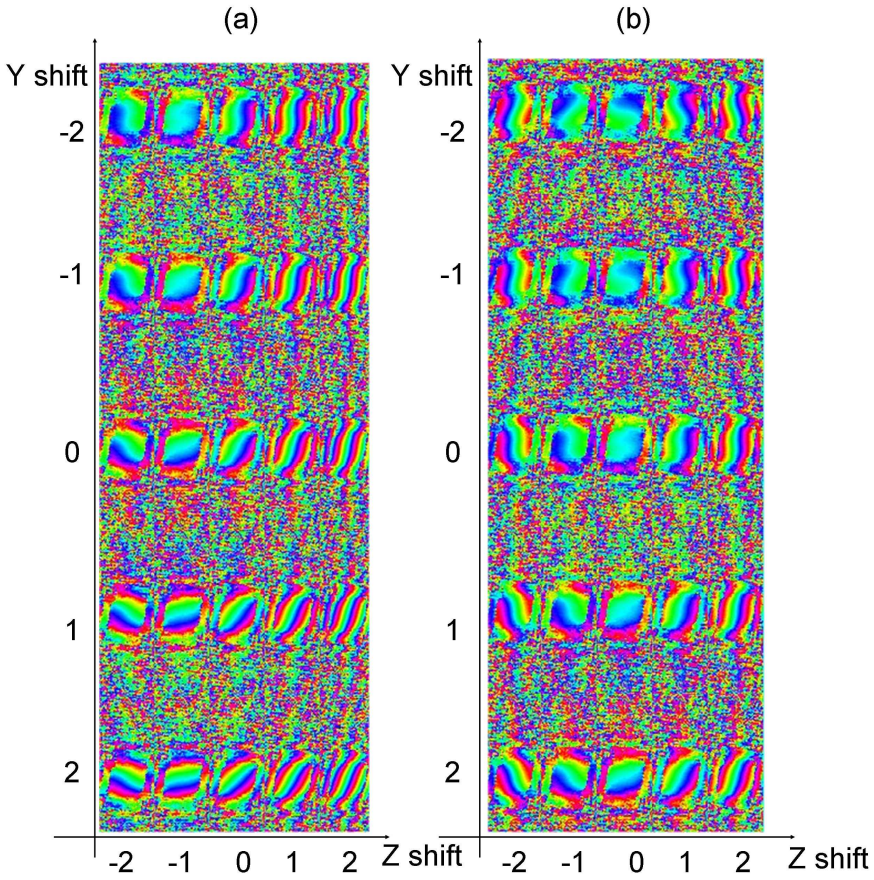

Figure 17: Autocorrelation of a 2D cross section of the 3D Dataset 27 in z-y plane pre (a) and post (b) centring, using 'dataCentre_5x5.py'

the required shift for a dataset to be identified quickly. In figure 17, a region of flat phase can be seen at a (-1 in z, -2 in y) from the centre of *(a)*, shifting accordingly leads to the centred result in *(b)*. The region of flat phase is not always obvious as the true centre of reciprocal space can lie anywhere in the 3D space a single voxel encloses, so slight gradients are inevitable but minimised using this method. It is also easier to use the gradients of surrounding shifts as they are larger, they give a clearer representation of the actual shift required, shown in figure 17 (b), moving clockwise around the largest shifts the gradients are radial to the centred position.

When centring it is important to buffer the data array with voxels of value zero, to the point whereby any shifts due to centring will not see the data wrapped to the other side of the array. If a dataset is incorrectly centred, the ability of the algorithm to find a solution is compromised as it bases the solution on a centrosymmetric diffraction pattern. The consequences of an incorrectly

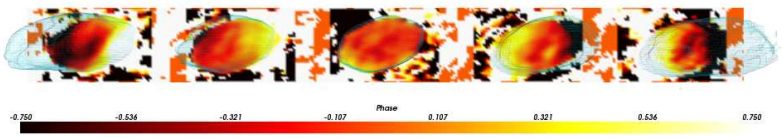

Figure 18: The reconstructed amplitude (translucent isosurface) and phases (2D scalar cut planes) for a phased dataset ±2 voxel variation about the central voxel in the x dimension

centered object are shown in Figure 18, large erroneous gradients from left to right appear across the reconstructed phase and the algorithm struggles to find a solution when ±2 voxels away from the true centre.

Once centred the user can decide whether or not to bin the data, there are two reasons to do this at this stage:

1. Save time in the data processing stage; maybe whilst carrying out an experiment to check the illuminated object is of reasonable quality.

2. Reduce the number variables the algorithm has to fit to, if a solution is not well defined the constraints are not tight enough. Binning reduces the strength of the constraint imposed on the data and allows the user to hone the constraints and scale up for the application to the raw dataset. After a reasonable support is chosen, the phasing operation can be re-run expanding the support in the required dimensions by the required binning factors.

Note, the autocorrelation function is also a representation of the object with extents approximately twice the size of the real object and will be used later to produce a constraint for the algorithms.

The data must be checked for 'aliens', erroneous intensity measurements due to cosmic rays, other crystals and air scatter must be removed as they too introduce asymmetry into the data, *see Section 4.3.4* for examples. These regions are simply cropped out by setting their value to zero, by 'alienExterminate.py'. The diffraction data is now ready for phasing.

The influence of nearby crystal diffraction tends to only affect the unfocussed mode of operation and is reduced by reducing the size of the beam incident on the sample and translating the sample to keep the crystal of interest in the beam.

Air scatter is minimised using a helium filled flight path from the sample to the CCD detector limiting the exposure of the beam to the atmosphere.

Another factor which cannot be ignored is the presence of transparent materials (Beryllium(Be) and Kapton) in the flight path, which can affect the coherence of the incident beam and interfere with the diffracted beam. Exhibited in experiments where the window lies between the diffracting sample and the CCD as the crystal is rocked in the beam a half-doughnut shaped artefact remains constant in position, seen in *Figure 19* left of the bragg peak. The artefact is present in every frame, is stationary relative to the sample but varies in intensity suggesting a stationary object inbetween the sample and the CCD.

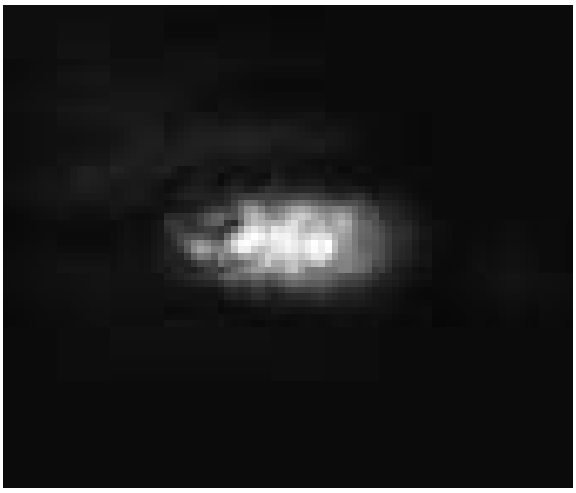

Figure 19: CCD image of a bragg reflection with Beryllium window induced doughnut shape

Both Kapton and Be exist in this region, the Kapton is attached to the detector arm therefore its illuminated area remains constant for all measurements. The Be window is large and different bragg reflections illuminate different parts of the Be window. Artifacts did not present in every diffraction pattern therefore the Be was the cause.

The data is now ready for phasing.

2.2.3 Phasing

The support for the data must now be chosen, this defines the region around the central position at which the real object is allowed to exist. From Section 1.2.1 the maximum size of the object is half the volume of the array. Generally, the datasets are oversampled by at least a factor of 2 in each dimension, so the support can be reduced to a quarter of the volume of the array. By observing the autocorrelation function (FT of the measured intensity is twice the size of the object) in 3D one can estimate the size of a rough support for the object. From experience, figure 20, this is set at 2/3 the extents of the autocorrelation function in each dimension. Large enough to find a preliminary solution but not small enough to impinge on the reconstructed object. The support can then be tightened further until it encloses the reconstructed object but does not interfere with its shape.

The reconstructed image is inspected and the support tightened or loosened depending on the effect of the support on the current output. This process has been sped up by feeding multiple supports to the phasing algorithm with variations of two voxel increases in each dimension (± 1 in the $\pm$ direction for each dimension to keep the support symmetric). Each dimension is approached independently, multiple dimensional variations in the support drastically alter reconstructions and lead to malsized supports and are difficult to converge. The programs used to complete this operation are 'varyXsupport.py','varyYsupport.py'

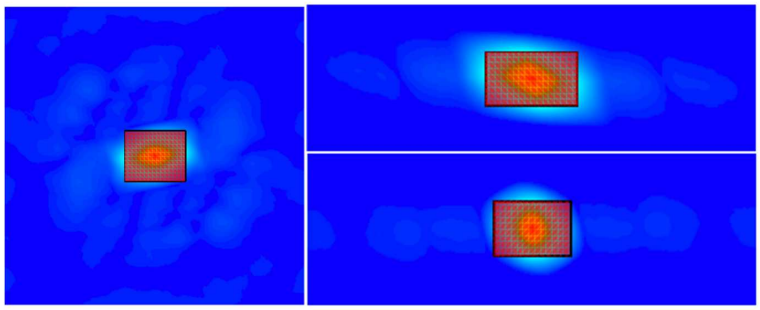

Figure 20: x, y and z slices through the autocorrelation function of a dataset and red wireframe isosurface of first guess at the support, approximately two thirds its size.

and 'varyZsupport.py'.

The reciprocal space constraint; the diffraction data itself and the direct space constraint; the chosen support, are fed into PC-HIO and ER algorithms.

The evaluation of the suitability of the chosen support is based primarily on the users intuition. To begin with the support is much larger than the object and hence can be changed dramatically to the users discretion. Once the user is no longer able to decide upon the variation required the χ^2 measure can be called upon but cannot be relied upon, equation 21. Figure 21 shows the progression of the χ^2 value as the PC-HIO algorithm proceeds for 50 iterations with a further 20 iterations of ER for several different sized supports, here B is the prime support, A is smaller than B by four pixels in each dimension, C is larger than B by two pixels in each dimension and D is larger than B by four pixels in each dimension. C and D both converge to a lower χ^2 than B, this is because the algorithms constraints are not enough for it to distinguish between solutions, a superposition of solutions result which can lower the χ^2, *see Figure 31.* Only A does not exhibit a saddle point (minimum χ^2) beyond which the PC-HIO algorithm, the constraints are too tight and force the solution to an erroneous state. B is determined to be the prime support as its reconstruction (Figure 23) has a relatively uniform amplitude distribution, well defined hexagonal facets and reasonably well defined ends, an estimate of the crystal dimension from the diffraction pattern also match the reconstruction, whereas C and D do not. C and D stagnate to a χ^2 close to their saddle point and are examples of the support being insufficiently tight for it to distinguish between its superimposed solutions.

Until this point the data is considered in voxel dimensions, in reality a geometric correction [2,21] provides a meaningful lengthscale for the reconstructed image in both reciprocal and direct space dimensions.

2.2.4 Theoretical Data Treatment

A simple three-dimensional model of the diffraction pattern of a hexagonal faceted nanowire was produced by Fast Fourier Transform (FFT); and is shown below in Figure 22. FFTs are simply efficient algorithms used to calculate dis-

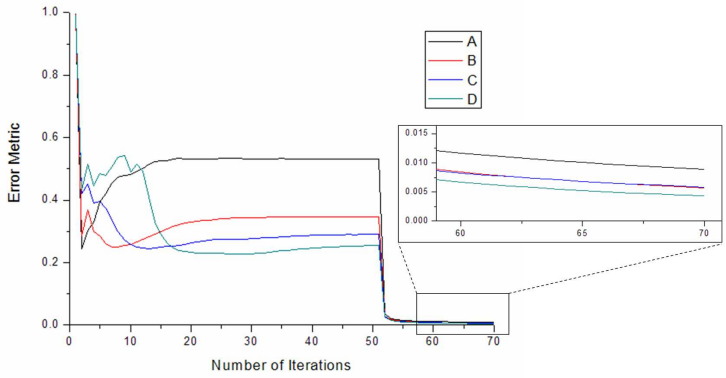

Figure 21: Tracking χ^2 for a phasing operation with multiple supports, where A < B < C < D

crete FTs and corresponding discrete inverse FTs. An experimental dataset is shown for comparison in Figure 23. The six fold symmetry due to the hexagonal cross section of the rod and two fold symmetry due the ends of the rod are evident, although in this particular case the two fold fringes are not well defined (are at the limit of oversampling). See Section 4.3.4 for an experimental example.

2.3 In-situ Experiments

2.3.1 Vacuum Chamber Setup

The unfocused setup discussed previously can be implemented in-situ; both for annealing and metal deposition evaporation experiments. The vacuum chamber is shown in *Figure 24*, the sample is clamped onto a ceramic heater, see *Figure 25* and has both vertical (z) and rotational (θ) translation when sealed into the vacuum chamber. The metal evaporator is located in the chamber loaded with Ni, Fe and Co sources. Diffraction from crystals on the sample exit the chamber through the large beryllium window highlighted in Figure 24 (b).

3 Results and Analysis

3.1 Zinc Oxide Nanocrystal Synthesis

The CVTD method used has been characterised. The temperature profile of the furnace is shown in *Figure 26*.

There are many variables which determine the morphology and size of crystals grown with this method they include; pressure, temperature, source material, oxygen partial pressure and the position of the substrate shown above. To an extent they all affect the amount of Zn supersaturate which oxidises in the gas phase to produce crystals. For uniform growth the amount of supersaturate needs to remain relatively constant for the growth duration. In practice this

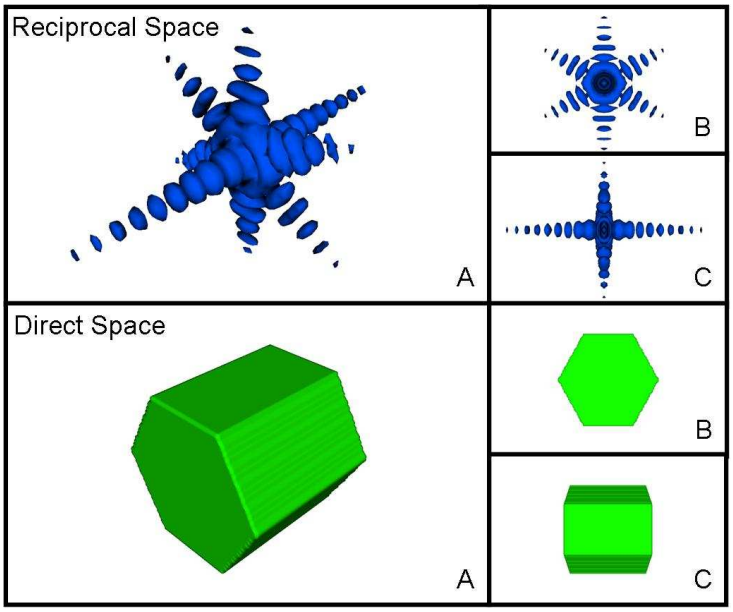

Figure 22: Theoretical reciprocal space diffraction pattern and corresponding direct space nanorod (a) Isometric View (b) Top View (c) Side View

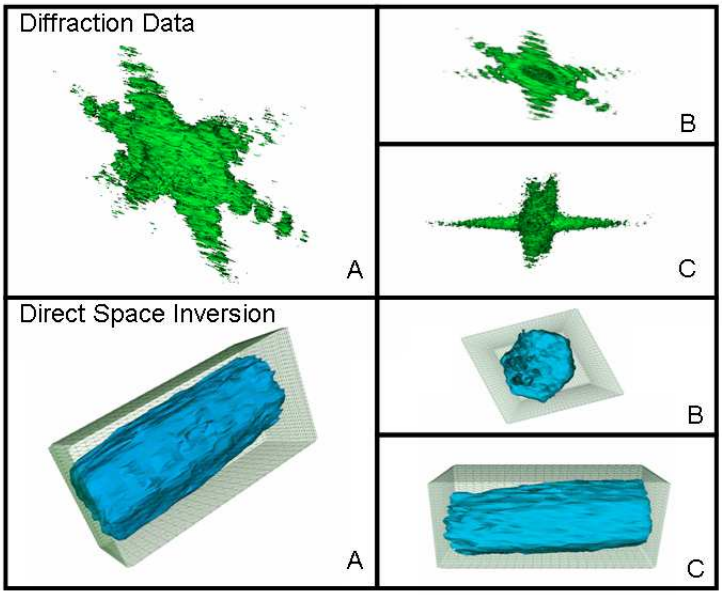

Figure 23: Diffraction pattern measured from a ZnO nanorod and corresponding direct space inversion (a) Isometric View (b) Top View (c) Side View

was very difficult, the conditions found to produce the most uniform crystals were 700sccm oxygen, 45sccm Argon, 1.5grams of 10:1 zinc carbonate to carbon ratio and the substrate positioned at 150^{o}C. An example of the variation in morphology of samples deposited at different temperatures is shown in *Figure 27.*

The rod morphology is deposited at 150°C (A) with little variation in size and morphology, upon increasing temperature a larger variation in structure was observed. At 190°C (B) few rods are deposited, balls of ZnO (up to 500nm) are observed in lines up to 10μm in length. At 270°C (C) nanowires (<100nm in width and up to 60 μm in length) are observed amongst other morphologies and at 420°C (D) high yields of ZnO whiskers are observed (tapered nanowires several microns long and less than 40nm in width).

The main drawback of vapour phase growth is the general lack of control. The material deposited was found to be heavily dependent on the gas flow in the tube, additional substrates in the tube caused deposition to change at different temperatures, Newton et al. [60] also proved this by using baffles to aid mixing of the supersaturate, producing the tetrapod morphology.

A solution to this problem is to catalyse the growth on the substrate at low pressures. To date Au and In catalysts have been used to seed ZnO structures, and can change the morphology of the ZnO. This method has the added advantage of adhering the crystals to the substrate and controlling crystal orientation as well as moving closer to the patterning of substrates for the mass production of ZnO devices. They also produce highly tunable aspect ratio's and uniform

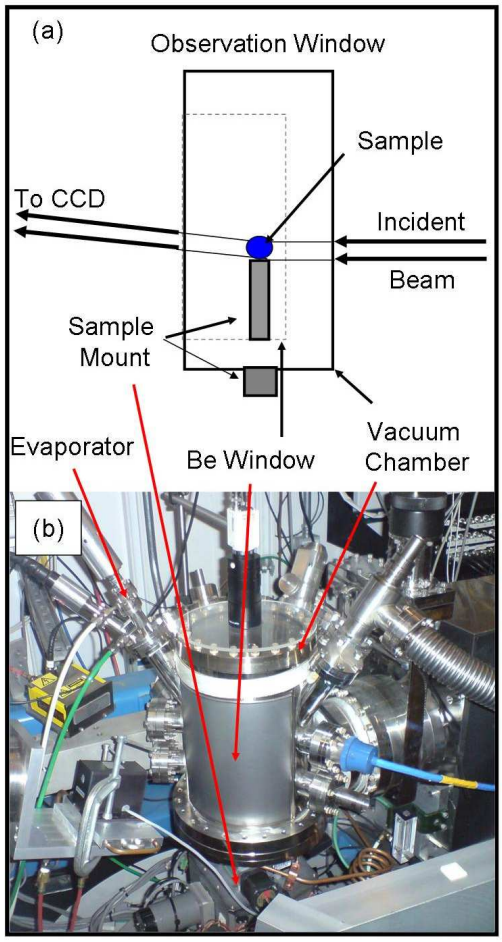

Figure 24: (a) Schematic of vacuum chamber (b) photograph

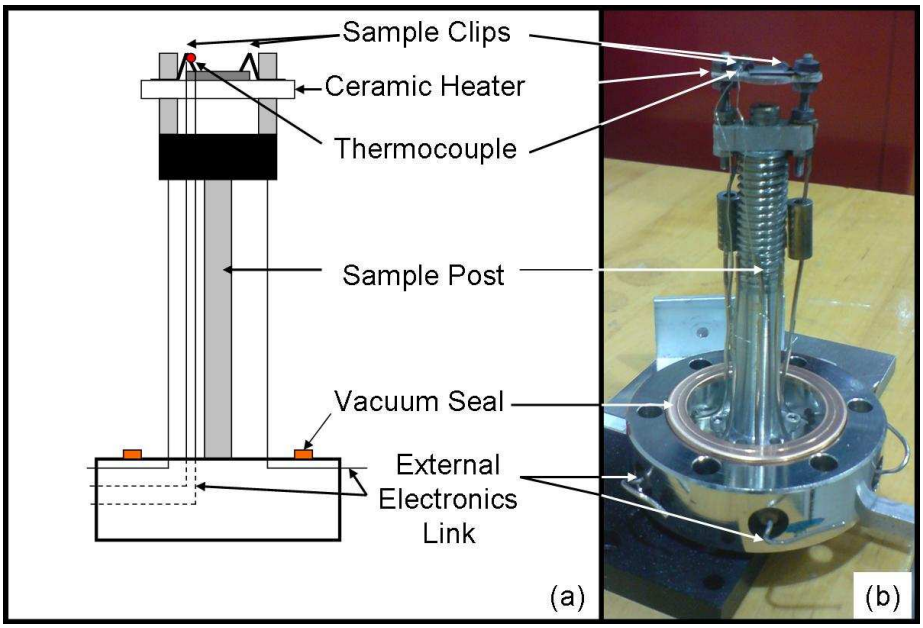

Figure 25: (a) Schematic of sample mount (b) photograph

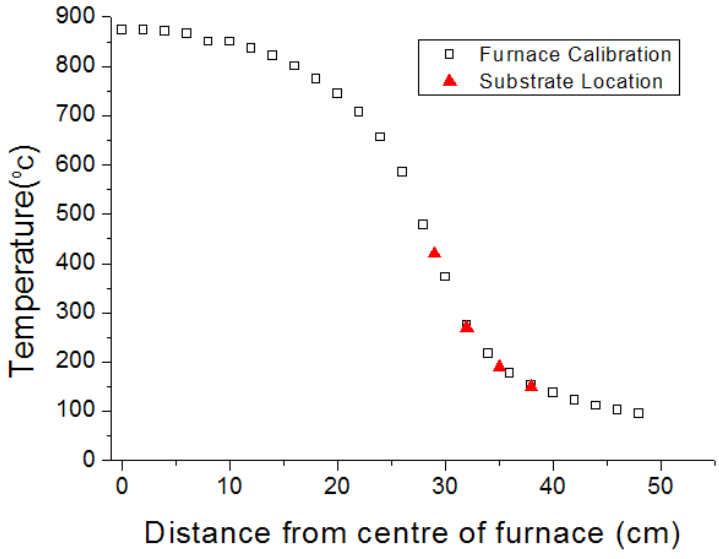

Figure 26: Temperature profile of the furnace system used to grow ZnO and locations of samples subsequently characterised with SEM

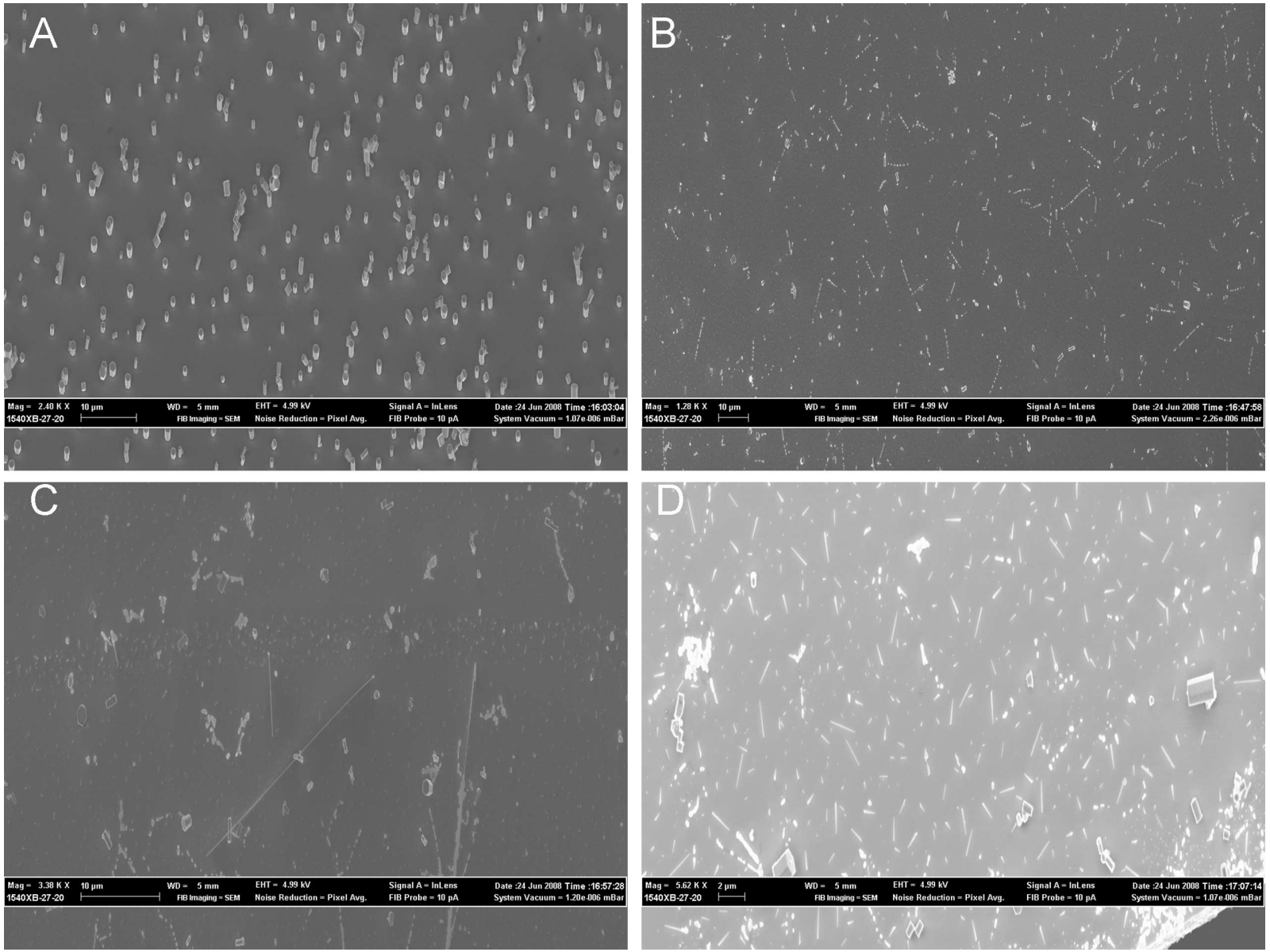

Figure 27: SEM micrographs of deposition structures at varying substrate positions (A) 150°C (B) 190°C (C) 270°C (D) 420°C

morphology across the substrate.

3.2 CXD ZnO

The phasing method described thus far, has been based on results from dataset 27. It encompasses a succession of improvements in the sample preparation, data collection and data analysis methods. A 3-dimensional render of the experimental data obtained by stacking up the 2-dimensional data and viewed in Mayavi (three-dimensional imaging software) is shown in *Figure 16*. The morphology of the rod is well defined (a) and (b) respectively; the two fold and six fold symmetry are evident, as seen in SEM. Increased rocking curves and smaller θ steps enhanced the resolution (b) of solutions. Subsequent 'alien' removal and phasing were carried out, the reconstruction is shown in *Figure 23*. The data was collected in beamline setup (2), see *Section 2.2.1*, with focusing mirrors, for an object greater in size in a single dimension than the beam, the beam itself defines the ends of the wire. Implying the edges of the focused beam are not uniform in shape and intensity. The subsequent smearing of the fringes in the 002 crystal direction could be explained by a rod with one well defined end and one rough end; manifested either from the algorithm itself, an erroneous feature or, the beam incident on either the base/top of the rod in which case the rod defines one end of the beam and the rough focus smears out the fringes. The preliminary results are very encouraging, a solid real object has been inverted from the diffraction data. Its dimensions have been estimated; width of uniform hexagonal facets between opposite parallel faces approximately 370nm and 700nm in length. This agrees quantitatively with estimates for dimensions and aspect ratios from SEM characterisation (although the exact crystal measured with CXD cannot be identified). Undulations in the surface of the reconstruction are of the order of the resolution of the image 50nm along the length of the wire and 40nm along its cross section. The important feature of the CXD technique is the ability to map displacements within the crystal, the phase maps shown in *Figure 28* demonstrate cross sections of the rod at 80nm intervals along its length.

Along the Q vector (101) direction highlighted in the cross sections consistently show a gradient from $+\pi/4$ to $-\pi/2$, the gradient is non-linear therefore a misalignment of the diffraction data can be ruled out as the origin of this feature but may be present underlying the non-linear feature. Observed in *Figure 17*, due to pixelation the dataset cannot be centred exactly so a phase gradient would be expected in most reconstructions and could exist as either an addition or subtraction from its current value. A suitable method for implementing this correction has not been considered to date, however the centring process should limit its effect. If a quadratic type phase structure were to be observed in experiments using a focussing optic the curvature of the wavefront would need to be considered as a possible source. Any phase structure described by a polynomial equation of the third degree or higher is likely to be a real phase feature.

In Figure 28 the positive phase in the positive Q direction corresponds to an expansion and equally a negative phase in the negative Q direction correspond to an expansion as well, this would be expected were oxygen vacancies found to be uniformly distributed throughout the rod and more pronounced as the vacancies increase close to the facets. Oxygen vacancies are expected in ZnO grown with the CVTD method and are the source of its n-type nature. There is

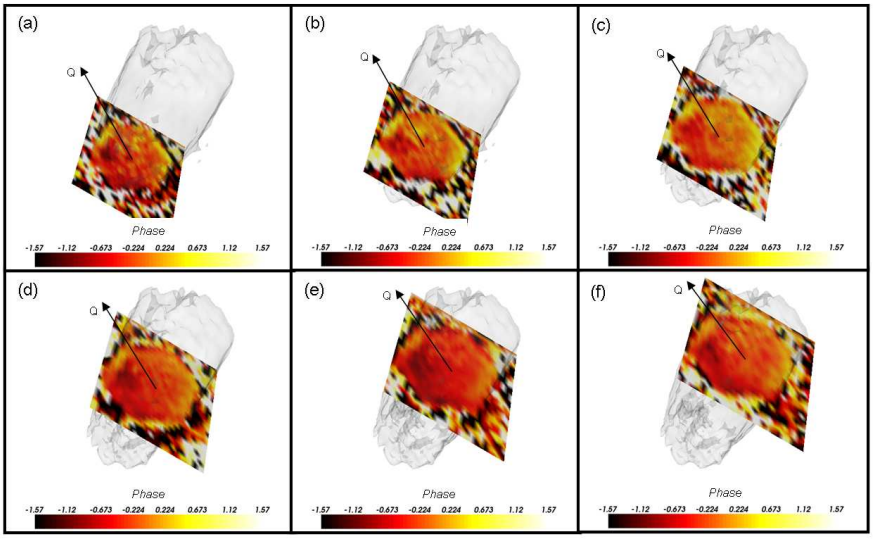

Figure 28: Phase map cross sections taken at 80nm intervals along the length of the rod (a)150nm → (f)550nm

no evidence to point towards a contraction on the surface due to the termination of the facets, the scale of contraction is likely below the resolution of the data so would not be observed. It is clear strains of some form have been observed but their origins are not clear. The proof of the hypothesis was the next step, if the strain was due to oxygen vacancies can we enhance this effect by altering the number of vacancies and observe the strains changing. The two obvious methods were to fill in the oxygen vacancies (oxygen plasma treatments) or induce more vacancies (annealing and metal deposition); the results are discussed in Section 4.3.

3.3 Variables in Data Collection

3.3.1 Binning

The CCD collates the readings from all the pixels from a user defined binning ratio into a single pixel on the computer screen. It requires an even number of pixels and can be set in the data acquisition stage or in the data processing stage. A compromise between data resolution, see section 1.2.1, and data collection speed must be reached. The Roper Scientific CCD can operate in two modes; fast and slow Analog to Digital Conversion (ADC) rates at 1MHz and 100KHz respectively. The associated name defines the speed of readout and each have a different threshold at which the CCD pixels register a photon count and saturate, a more limited dynamic range in fast operation mode. A high resolution comparison has not been made, but low resolution data has shown no difference between the two modes of operation, hence the fast ADC was used. Once the oversampling ratio has been satisfied the acquisition speed is maximised by binning the data to the point where the oversampling ratio is

met. The resolution of the dataset is defined by the statistics in the n^{th} order fringes, where n is an integer the resolution is defined by the crystal extents d in dimension of fringes divided by the number of observable fringes, d/n. The resolution is therefore set by the acquisition time, through experimentation and the need for good statistics this was set to 200+ accumulations of each pixel at an exposure time defined by the brightest part of the bragg peak at 80% pixel saturation.

3.3.2 Weighting

When large crystals are observed their diffraction patterns are very intense. The detector can be moved further away from the sample spreading the intensity across more pixels increasing the readout time. Alternatively attenuators (Molybdenum or Aluminium, depending on attenuation factor) were required to protect the CCD and beam stops cover the brightest region to obtain good statistics in the outer fringes of the diffraction pattern quickly. In both cases the different frames or different parts of frames of a diffraction pattern carry different weights, *see Figure 29*; a rocking curve taken through a ZnO Bragg reflection using attenuation of 50μm Mo, 25μm Mo and zero attenuation moving from the centre to the outer fringes respectively. An attempt to scale the dataset failed for three reasons:

1. The predicted scaling factor did not match the scaling factor required at corresponding attenuation steps.
2. Where large attenuation and short exposures were used large amounts of data was lost at high Q, it is impossible to scale a count rate of zero.
3. Drifting of the sample during measurement is non uniform because the number of accumulations and CCD exposure time were different for each attenuation.

The method for scaling for attenuators was explored further with the use of beamstops. Beamstops create an equally difficult problem whereby the alignment of the beamstop to the CCD is not perfect and overlapping pixels make it difficult to scale accordingly. The ambiguity of the attenuation provided makes it very difficult to successfully match statistics accurately between frames of different attenuation and can completely suppress low intensity data in the outer fringes. Beam stops have been used successfully in CXD microscopy and incorporated into iterative phase retrieval algorithms [71, 72].

3.4 Algorithm Constraints

The user defined algorithm constraints will be discussed in this section.

3.4.1 Threshold

The threshold is an addition by Ross Harder, applied to the phasing algorithm so that all data below a certain value should be ignored by the algorithm. This threshold is determined by the user and is usually set to several photons. The CCD detector outputs the measured intensity in Analog to Digital Units (ADUs), a full discussion of the operation of a CCD detector was provided

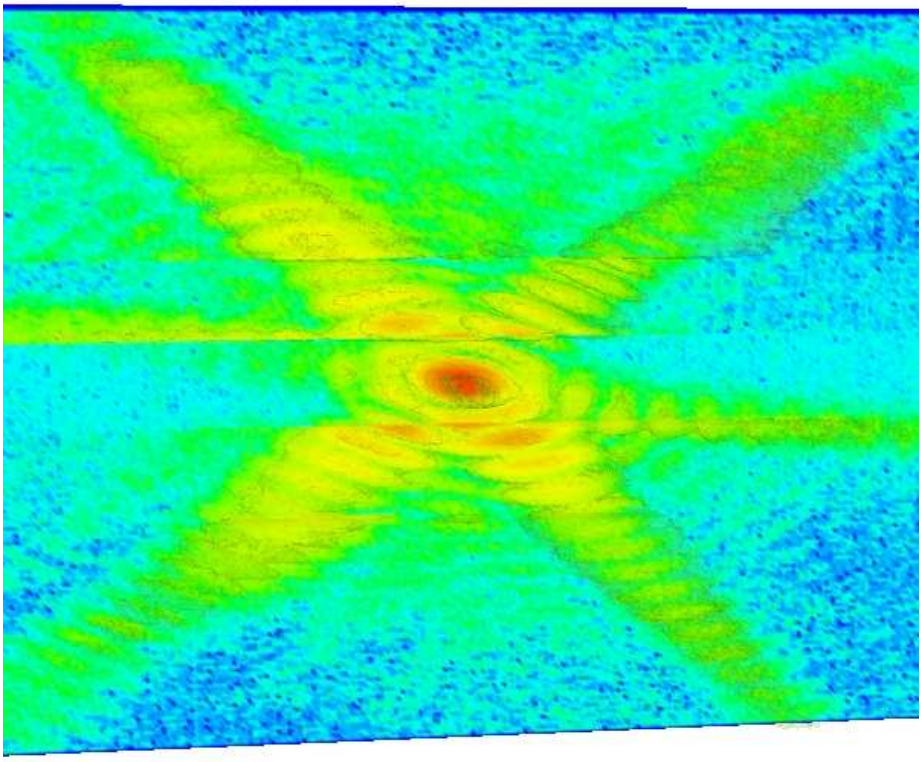

Figure 29: Scalar Cut Plane of the amplitude across a concatenated diffraction pattern 3 levels of attenuation were used (zero, 25um Mo, 50um Mo)

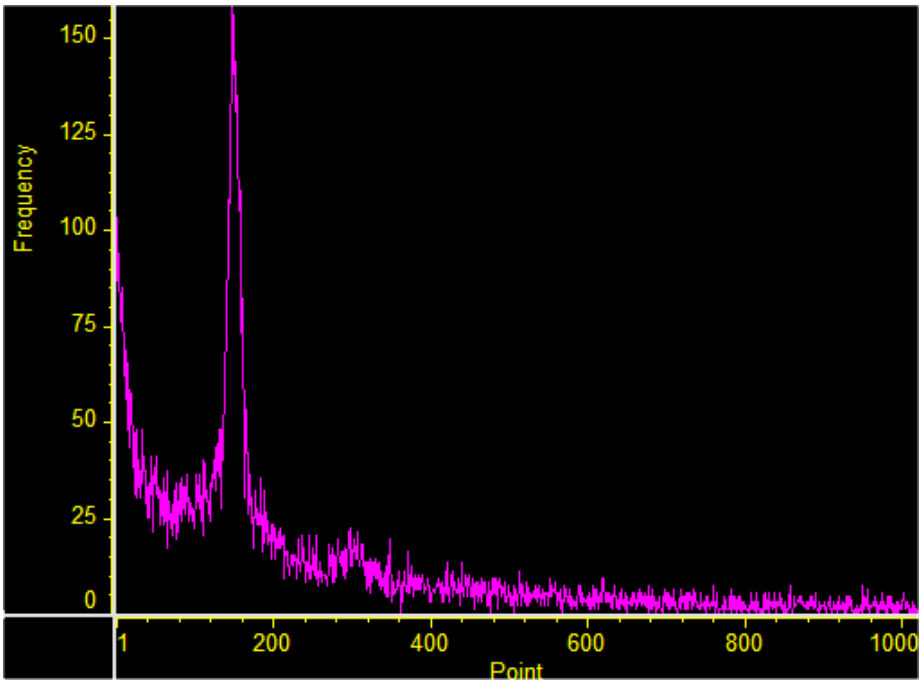

Figure 30: Histogram produced in WinView (Roper Scientific) for DS_{131} identifying the frequency of intensities measured on the CCD

by Howell [73]. The gain of a CCD determines how the charge collected in each pixel will be assigned to a digital number. As the majority of intensity measured surrounds the Bragg peak, low intensity regions will register single photons. Histograms of these regions identify single photon and sometimes double photon peaks. Figure 30 illustrates a prominent single photon peak of the order 140-150 ADUs and a double photon peak observable only in the 2D slice taken through the Bragg peak of 320-370 ADUs respectively.

The effect of the threshold is very important. When set too low and the algorithm is forced to represent a large number of low intensity pixels leading to stagnation and if set too high the resolution of the image is compromised. However, this feature can be advantageous, by setting the threshold deliberately high the algorithm reconstructs a low resolution object, easier to converge due to fewer data points and a good starting point when approaching datasets that stagnate at lower thresholds.

3.4.2 Masking/flagging

A method favoured by Mark Pfeifer [3], it is a method similar to that of the threshold whereby it aims to remove erroneous data from the algorithm of the similar intensity to real features present in the diffraction. A manual technique whereby individual regions of the diffraction pattern are identified and removed from the diffraction data one 2D frame at a time. It becomes essential when the presence of alien crystal diffraction is recorded when the rocking curve is

taken, this must be excluded from the algorithm for it to realise the true crystal structure. This is currently implemented using 'alienExterminating.py' in 3D see *Section 2.2.4*. For dataset 27 a large number of 'aliens' were removed, down to individual erroneous pixels; a time consuming process required to eliminate large contributions to error metrics for very similar solutions.

3.4.3 Iteration Number

HIO was touted by Marchesini as the most powerful algorithm, and has been found to be very good at phasing 3D diffraction data. The behaviour of this algorithm is intriguing, as shown previously in Figure 21. The chi square value drops before stagnating at about 0.2, the value it stagnates to is dataset dependent and a property of the amount of binning but does not scale with binning ratio. The output of the algorithm at each iteration is shown in figure 31A, beginning with a copy of the support the algorithm proceeds to a state of two overlapping solutions and then converges to one of these solutions. Cross sections of the amplitude, shown in *Figure 31C*, show two 'hot spots' (red) superimposed onto one another with a small offset, these 'hot spots' merge until the algorithm imposes a change large enough to move into another local minima in solution space. The reconstruction concludes a highly nonuniform amplitude distribution. This behaviour is common in the HIO stage of the iterative process and no more than 35 iterations are required to find a preliminary solution. In the preliminary stages of phasing when the support is being shrunk more iterations are sometimes necessary, however the existence of the minimum in the error metric after several iterations is used to identify when the support is starting to reach a reasonable size.

3.4.4 Start Point

The iterative algorithms employed require an initial guess of the shape of the crystal and comes from the determination of the support. If the algorithms are robust enough to find the global minima, the solution should be independent of the starting point. A simple test for this is replacing the support region (defined as a region of 1s) by random numbers. Random starts do not always produce the same solution and highlight the ambiguity problem , see *section1.2.2*, a stonewall test for the reliability of the result. Ambiguous solutions are also a good indicator that the solution is the correct one and ambiguities can be checked by carrying out cross correlations between images. Cross correlations simply raster images across one another until they coincide, inspection determines similarity, or if there are multiple solutions the cross correlation itself determines the identical solutions. A cross correlation method similar to this is employed in the guided HIO algorithm [23] to identify similar traits between solutions. The method is demonstrated in Figure 32, here two 3D images of cubes g(x,y,z) and h(x,y,z) (left) at different locations in an array are superimposed onto one another. Combination of their Fourier Transforms provide a correlation map from which the required shift to map one image onto the other is extracted, shown on the right by a wireframe representation of g(x,y,z) now superimposed onto h(x,y,z).

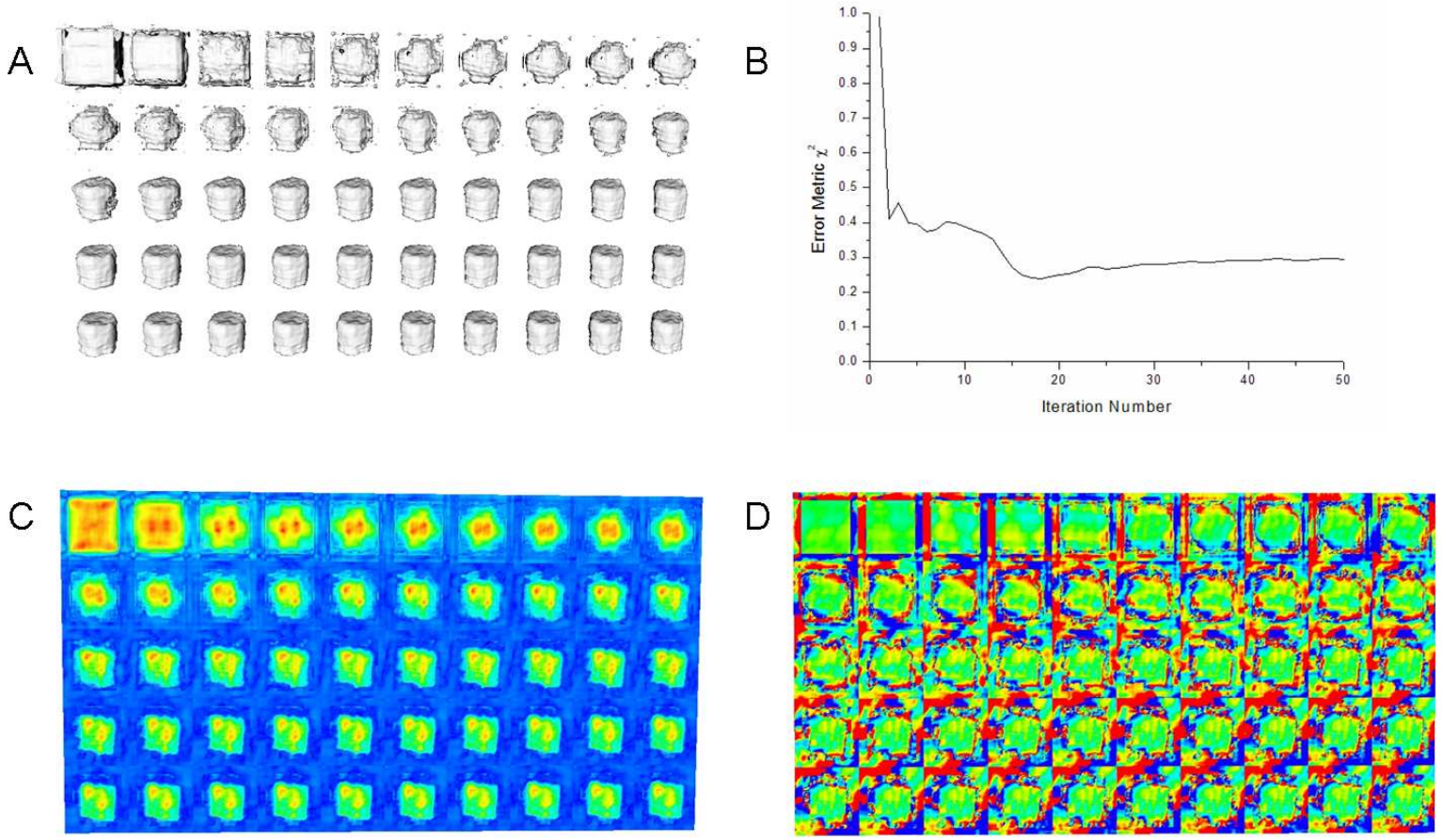

Figure 31: An isosurface of the amplitude (A), the error metric (B), scalar cut planes of the amplitude (C) and the phases (D) are displayed for every iteration of a 50 iteration HIO phasing operation carried out on dataset 62 (April 2008)

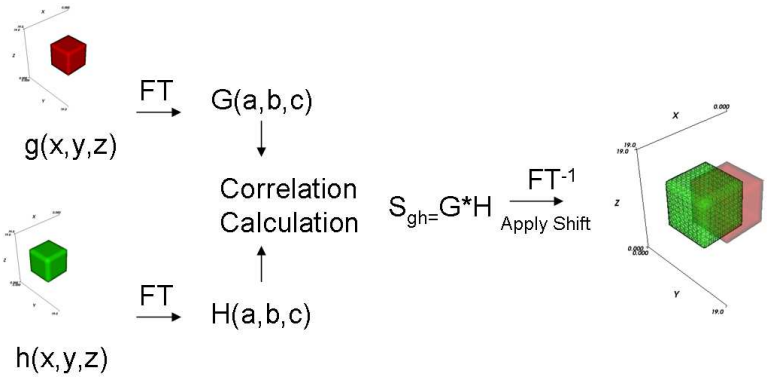

Figure 32: Fourier Transform cross correlation method

3.4.5 Support Choice

The support construction is based around the volume enclosed by a set of defined planes. At present, depending on the number of defined planes a large portion of the support will in fact remain empty. Therefore the algorithm has only the raw diffraction data to constrain it in these regions, in reality the constraint could be tighter. These regions of empty support become significant when the crystal lies at an angle to the pixels and in the worst case scenario at 45^o to every dimension the support has a volume four times larger than the ideal scenario. Using rotated planes is time consuming and but as expected significantly improves the convergence of the algorithm. This process is not automated at present, a proposed shrinkwrap algorithm [20], uses the autocorrelation function to begin with and smooths the function, constantly updating the support relative to the solution. Ideally this should make the support as tight to the reconstructions shape as possible but has one significant drawback, by updating the support relative to the solution the solution drives the support so the algorithm will always produce the same result. Effectively the robustness of this algorithm cannot be easily tested as the starting point is predetermined. The variables for the smoothing and building the new support define the random nature of the solution, it is not obvious what these should be determined to be. From experience the support has the most impact on the reconstruction and when asymmetric can favour previously ambiguous solutions. For the application of such an asymmetry *a priori* knowledge is required, if it is not possible ambiguous solutions should be dealt with via cross correlation.

3.5 Common Problems

The inherent problems in reconstructions emanating from the constraints placed on the algorithms will be discussed.

3.5.1 Uniqueness

The indirect Fourier Methods used to phase diffraction patterns have an intrinsic drawback, there can be multiple solutions to a single problem, *see Section 1.2.2.*

The Fourier Transform of the two objects are identical, in Figure 33 A and C are twinned 2D shapes and the fourier transform is the same for both. Raising the question; How does the chosen algorithm come to a suitable conclusion? The answer should be; it should not produce a single solution (see *Section 3.5.2*) as all solutions are equivalent, instead they need to be compared to find agreement therefore making the solution viable.

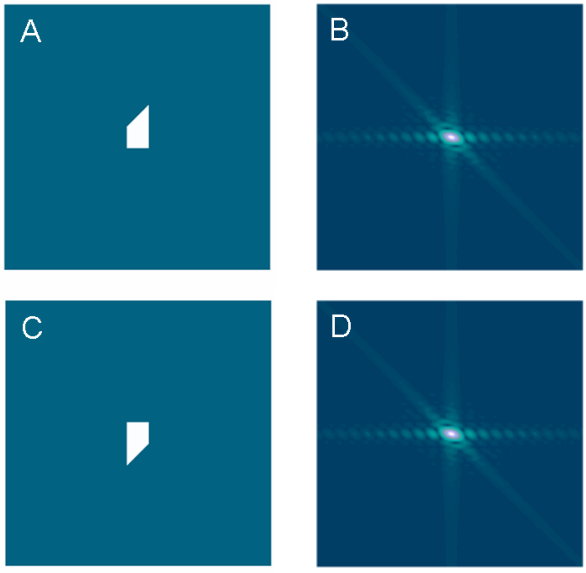

Figure 33: A crystal (A), its twin (C) and the corresponding reciprocal space representation via FT (B) and (D)

It is generally accepted that multiplying the support (our best guess of the object) by random numbers and beginning the phasing process from this point should lead to the correct solution more frequently (>50%). As twins are effectively the same solution they must be identified, a method for achieving this is via cross correlation, see *Section 3.4.4*. Rotating one solution 180 degrees about two axes will move the two solutions into the same frame of reference as its twin. Cross correlating the two reconstructions is necessary as there is no guarantee they will lie in the centre of the array. A visual comparison or numerical bandwidth can determine if they are in fact twins. When twins do not exist the constraints on the object are deemed too small and need to be reconsidered.

3.5.2 Stagnation

Stagnation describes the point at which the algorithm can no longer instigate a change to the result based on the defined constraints large enough to change the solution and is identified when the χ^2 never drops below/ oscillates in close proximity to a value. In Figure 31 after 25 iterations of HIO χ^2 settles near to

0.3. In this case the algorithm constraints have been fully optimised. In solution space this can be thought of as oscillating around a local/global minima, subsequent iterations of ER are used to clean up the solution and find the minima. Stagnation can also define the scenario at which the algorithm cannot decide between two ambiguous reconstructions and instead outputs a superposition of the two reconstructions.

4 In-situ Metal Deposition

4.1 Motivation

To confirm if the phase result obtained in *Section 3.2* were a result of the presence of oxygen vacancies the samples were treated with oxygen plasma to fill in the vacancies and relieve the strain. The inability to carry out the experiment in-situ held no guarantee the sample would remain in this state until measured. At 34-ID-C a Ultra High Vacuum Chamber (UHV) can be used to anneal and evaporate metals onto samples, this would increase the density of oxygen vacancies and the strain across the nanorods. ZnO samples were annealed to 700°C and an expansion due to annealing was observed as expected. This was large enough to move the diffraction completely from the detectors field of view and meant close tracking of the crystal during annealing was required to ensure the same crystal was measured. Inspection of the diffraction pattern alone determined no variation in intensity around the Bragg peak; subsequent reconstructions confirmed no obvious structural change, but provided the following conclusions:

1. The crystal remained on the sample during the annealing process, therefore oxidation as a method of adhesion was successful.

2. The crystal became unstable above 600°C therefore any data beyond this was compromised.

This prompted a more vigorous approach to introducing strain, the deposition of more electronegative metals onto the ZnO to induce oxygen vacancies at the surface. The metals deposited included Iron (Fe), Nickel (Ni) and Cobalt (Co) all whose electronegativity according to the Pauling Scale [74] is greater than ZnO, shown in the table below.

Table 1: Electronegativity based on the Pauling Scale for deposition metals [75]

Element	Zn	Fe	Ni	Co
Electronegativity (Pauling Scale)	1.65	1.83	1.91	1.81

For an average size ZnO rod (0.7μm x 1.5μm), a 14nm deposition would be required to sufficiently dope the rod to the suggested soluble limit $Zn_{0.93}Fe_{0.07}O$. The solubility of Fe in ZnO ranges has been reported in the range 2-7% [76–79] beyond which secondary phases Fe_3O_4 were observed. Lattice parameters for Fe doped ZnO have been measured for 1%, 3%, 5% and 7%, at 7% a=3.2547Å leading to an expansion of 1.23nm across the width of the crystal corresponding to a 7π expansion. Controlling the dopant level is within the resolution of

the CXD technique, as yet data with phase wraps beyond 2π have not been recovered but simulated to match diffraction data by Gailhanou et al. on silicon on insulator lines [80].

4.2 Method

The deposition experiments were carried out in the vacuum chamber, see Section 2.3.1. The unfocused mode of operation required larger rods to be grown, the growth parameters were tailored to produce rods between 0.5-2μm in width and 1-5μm in length (700sccm Ar, 45sccm O_2, source at 867°C and substrate at 150°C). As seen previously in Figure 12 (a) lines of ZnO crystals are present, each deposition line consists of crystals of similar morphology, in some cases the majority (>80%) of rods were stood on end. The density on the surface is high for a (20μm x 20μm) beam footprint (>5) but the deposition growth method ensures they are not aligned to the substrate as they are grown in the gas phase; the substrate orientation has shown no influence on the crystal orientation, if multiple crystals are illuminated interference between diffraction patterns is less probable. The oxide layer was grown to 50-100nm to adhere the crystals to the substrate, deviations in the oxide surface near the nanorods must be considered when understanding the strain present.

The crystals were then measured, heated to 200°C and metal deposited to between 10-100nm, the sample was then heated and measured at each temperature in a stepwise fashion up to 600°C. The deposition was carried out at higher temperature to reduce the risk of losing the crystal being measured due to thermal expansion of the sample mount, not just the expansion of the crystal.

4.3 Preliminary Results

4.3.1 Experimental

Initial observations of the Bragg peak of a ZnO nanorod post Fe deposition and annealed for two different samples 108A and 115 are shown in Figures 34 and 35 respectively.

The crystal has decreased in size as the interference fringes have become larger, therefore a reaction between Fe and ZnO has taken place. A relatively low temperature of 350°C considering Bates *et al.* [79] observed a solubility of zero at 500°C increasing as a function of temperature to 7% at 800°C. A solubility of this order does not explain the large variation in diffraction. The low temperature observed can be explained by heating of the nanocrystal due to the illuminating beam and the presence of large errors in the temperature measurement. The thermocouple sits several millimetres away from the illuminated region of the sample. Inspection of the silicon as it began to conduct suggested a good temperature calibration the sample began to glow orange at 600°C, *see figure 36.* The heating was asymmetric, large gradients were evident across the sample. The thermocouple resides on a mounting plate attached to a screw hence, measures a different temperature compared to that of the illuminated sample region. Error in the thermocouple itself must also be considered, they are less sensitive at higher temperatures as they exhibit a negative exponential resistance to temperature relationship.

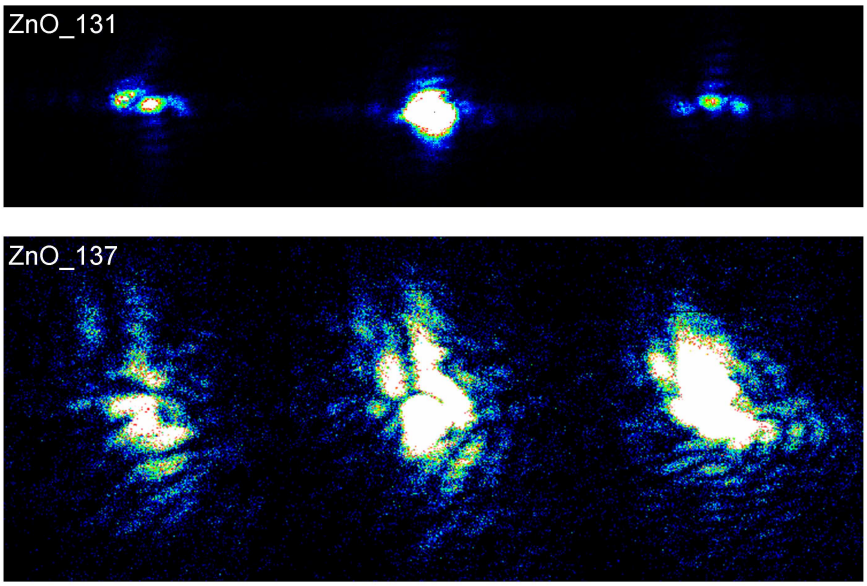

Figure 34: Diffraction data at -4,0,+4 frames offset from the bragg spot at (a) 298°C (DS_{131}) and (b) 358°C (DS_{137}) for sample 108A

The structural change was later confirmed with SEM, Figure 37. Sample 108A was heated through to 350°C and post experiment SEM analysis shown in A and B confirms the presence of crystals coated with a layer of Fe. Sample 115 was heated to 600°C shown in C and D, the layer of Fe has dewetted the surface and the internal degradation of the crystals can be observed. Confirming the observations from the x-ray diffraction data and highlighting the ability of CXD to observe the reaction proceed.

Further experiments were carried out with Fe, Ni and Co depositions ranging between 5-100nm.

4.3.2 Phasing

4.3.3 Fe (Sample 108)

Diffraction patterns were measured for a ZnO crystal at the (101) Bragg reflection predeposition (DS_{131}), post deposition (DS_{133}), at 298°C (DS_{135}) and 350°C (DS_{137}). Reconstructions from the subsequent phasing process are shown in *Figure 38* and the corresponding raw diffraction data are shown alongside the reconstructed diffraction data (Fourier Transform of the reconstructed direct space solution) in *Figure 39*.

DS_{131} proved difficult to reconstruct, the reconstruction has a well defined non uniform hexagonal cross section with rough ends. In the raw diffraction pattern the fringes that correspond to the hexagonal cross section are clear whereas those corresponding to the ends of the rod are barely visible. The presence of two satellites and diffuse scattering local to them on the left and right of the

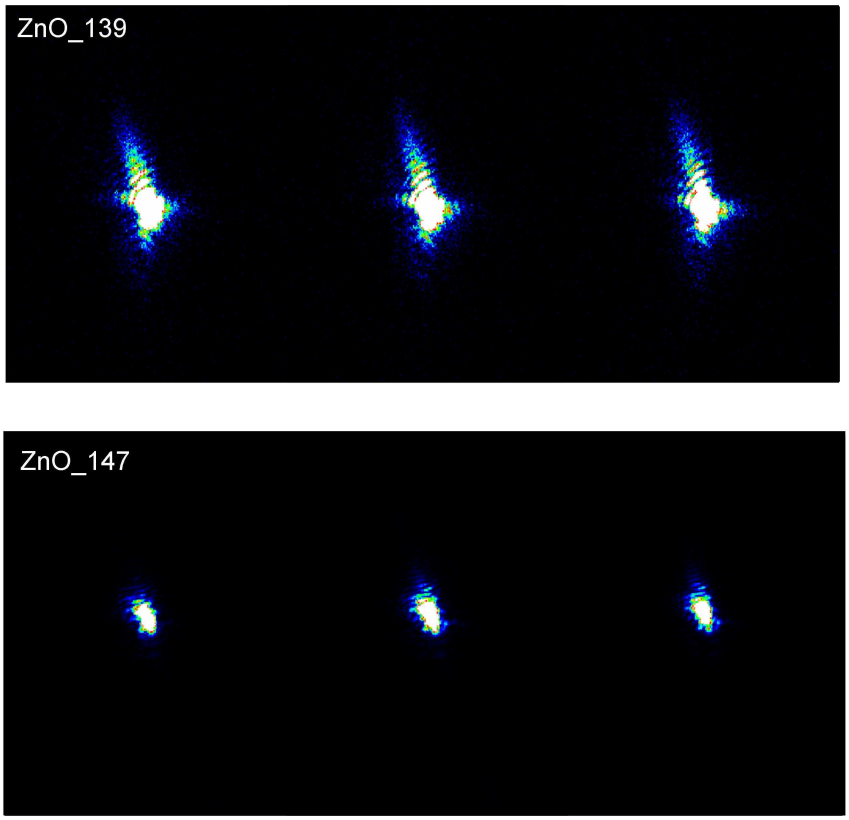

Figure 35: Diffraction data at -1,0,+1 frames offset from the bragg spot at (a) 230°C (DS_{139})(b) 400°C (DS_{147}) for sample 115

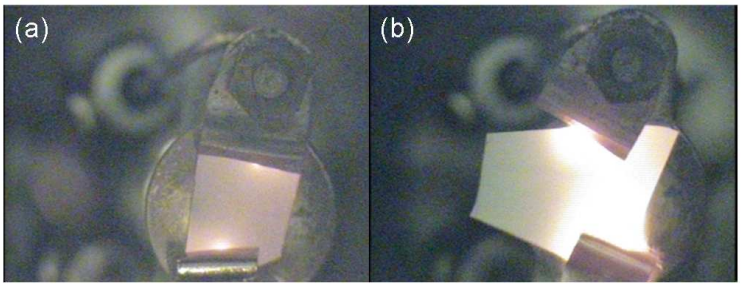

Figure 36: Silicon wafer mounted and heated to approximately (a) 600°C and (b) 780°C

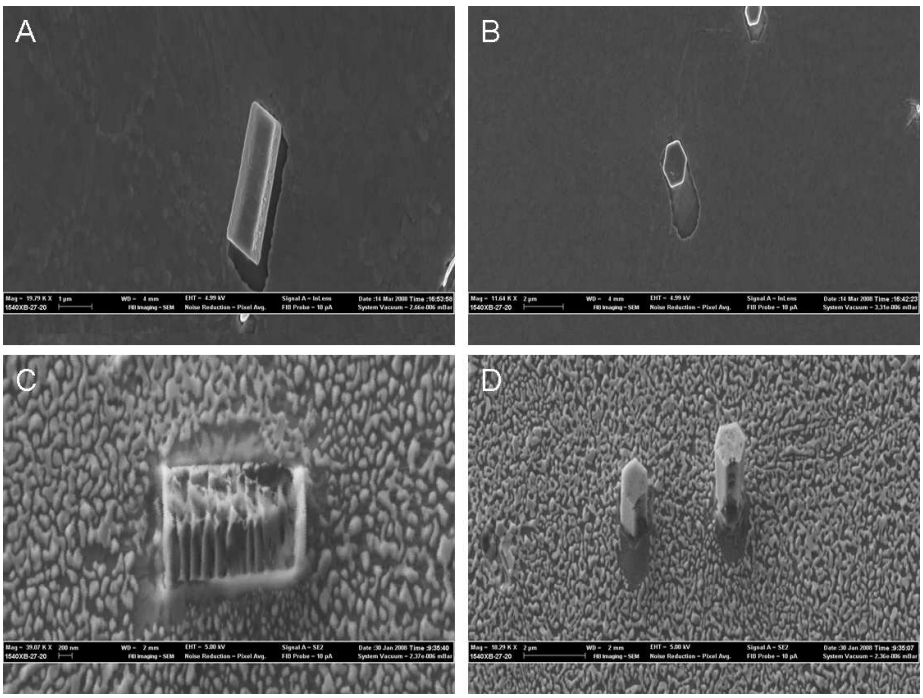

Figure 37: SEM from sample 115 (A and B) and sample 108 (C and D) for two different orientations of crystal imaged by CXD

Bragg peak are evidence of a failing shutter system. As the ADC read out the shutter shut sporadically leading to additional exposure of the CCD chip during readout and was only observed in the central frames where the intensity was significant. This was confirmed by shutter tests and the problem amplified by rotations away from horizontal operation (preventing certain Bragg reflections from being measured). The error was significant as it was reconstructed in the phasing operation, the solution is therefore incorrect and cannot be improved because the diffuse scattering impinges on the diffraction pattern itself. Removing it, as we have done previously with cosmic rays etc, is not feasible as it adds to the diffracted intensity and we have no reference measurement to subtract it correctly because the number of failures per frame is not known.

Two reconstructions of DS_{133} are shown. Firstly, the dataset was reconstructed with a cosmic ray present (highlight by a red circle in the diffraction pattern), here the phasing process reconstructs the cosmic ray and a second transposed version. Secondly, it was reconstructed with the cosmic ray removed. The reconstruction with the cosmic ray removed has a more uniform amplitude distribution than the reconstruction without, yet still possesses a well defined cross section and rough ends. This highlights the importance for the removal of all erroneous data from the measured diffraction patterns as only 7 erroneous pixels have impacted the reconstruction.

The reconstruction of DS_{135} is arguably worse than the previous datasets, but there is no definitive method of identifying if it is the reconstruction process or the data itself that has created this variation.

DS_{137} is completely different to the previous reconstructions as expected from the variation in the diffraction data, the top and side views show the crystal is now very different. There is agreement in the size of the object in the cross section dimension between all reconstructions, although practical identifiers are no longer obvious to the naked eye.

The resolution of the reconstructions is defined by the number of visible fringes, in these cases 8 fringes across the width of the rod and 8 fringes along the length of the rod. The width and length of the rod was measured to be 908nm and 1406nm from DS_{133} and 817nm and 1492nm from DS_{135} using the point Picker module in Mayavi. The resolution of the reconstruction ($\frac{crystalsize}{numberoffringes}$) is 113nm across the width and 175nm along the length of the crystals. To improve this the total exposure time must be increased and attenuators must be removed. The addition of attenuators affects the whole diffraction pattern uniformly, as shown in *Figure 29* on page 36 whereas we only require attenuation within one or two fringes of the Bragg spot like the beamstop method discussed in Section 3.3.2. To overcome the limitations of a beam stop method and the persistent shutter problems experienced, a laser shutter was mounted on the diffractometer reducing the allowed exposure time from 0.1 seconds to 4 milliseconds, the attenuators were removed as single exposures no longer saturated the CCD.

The integrated intensity will remain constant for the diffraction data if the variation in crystal structure is strain based because the number of electrons responsible for diffraction around the Bragg peak remains constant. If the crystal structure was changed dramatically i.e the Fe reduces oxygen from the ZnO leaving amorphous Zinc and FeO crystals behind a drop in intensity would be observed. DS_{131} = 7.60x10^8ADUs matches DS_{133} = 7.62x10^8ADUs when it shouldn't if the shutter operation had improved, DS_{135} = 8.9x10^8ADUs shows

a 17% increase that cannot be explained (a beam refill at the synchrotron is insufficient to account for this error), whereas DS_{137} required longer exposures to observe reasonable statistics DS_{137} = 6.27x10^8ADUs therefore the crystal structure has significantly changed. This is confirmed in the diffraction by the increased fringe spacing and translates to the reconstructions as a much smaller, strained crystal.

In general it is clear from the reconstructed diffraction patterns a significant amount of noise is present relative to the raw data. In the reconstructions fringe definition is worse but the algorithm has made good progress on reproducing the dataset. In light of these observations an improvement in statistics was sought in the form of more accumulations with added resolution for the reconstructions.

4.3.4 Fe (Sample 115)

Reconstructions of datasets DS_{139}, DS_{142}, DS_{144} and DS_{147} from sample 115 are shown in *Figure 40* and the corresponding raw and reconstructed diffraction data are shown in *Figure 41*.

DS_{139} did not reconstruct, all variations produced a similar irregular object which remained attached to one side of the defined support. There are several possible explanations. Insufficient statistics cannot account for the morphology as there is significantly more statistics than that obtained from sample 108. The crystal was aligned with a peak intensity of 4.50x10^4 ADUs, therefore for 100 accumulations we would expect a peak intensity of the order 4.50x10^6, a peak intensity of 4.04x10^6 was observed so the crystal may have moved slightly during the scan rendering the dataset defunct. In this experimental set up we have no method for identifying variations in the incident beam intensity, this can have large consequences on the data collected, variations can arise from several sources including beam refills and fluctuations in beam position. As the length of the scan is increased the data is at greater risk from these problems.

DS_{142} reconstructed well, the object has a well defined hexagonal cross section and two well defined ends, one flat and the other missing a divot. The divot has an associated phase structure shown in fig.41 that will be discussed later. A cause for concern can be seen in the reconstructed diffraction data, a very close alien was removed and some of the diffraction data was sacrificed as well, the phasing operation reconstructed the hole in the data rather than filling it in. By setting a threshold the algorithm has free reign over all voxels below the threshold, hence it should not try to force these values to zero to converge the algorithm, or consider these voxels in the error metric calculation. Further analysis found the phase structure to be a property of the diffraction data, by increasing the threshold the sharp edges in reciprocal space were removed from the diffraction data and the same phase structure observed.

DS_{144} reconstructed well, again a well define hexagonal cross section, one very flat end and the other is well defined but not as flat with a smaller phase structure. This reconstruction exhibits the phase structure on the opposite end to DS_{142} suggesting one of the two is a twin to the correct solution but is impossible to tell which is correct. A best guess would assume some form of substrate crystal interaction due to the oxide layer growth. The phase maps from DS_{142} show a large phase variation at the top of the structure and an increase in phase towards the edge, specifically for the 90°,120° and 150° examples. If indeed the crystal is embedded in SiO_2 to some level estimated to

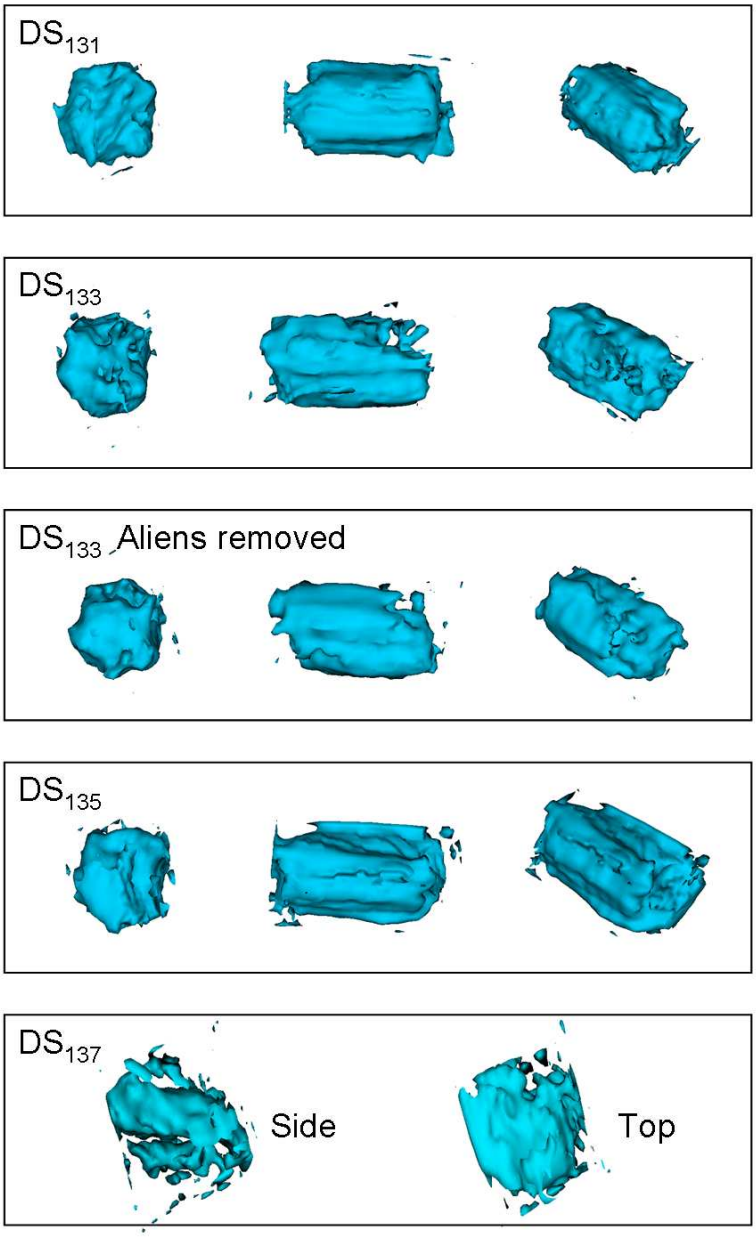

Figure 38: 3D renders of reconstructions for DS_{131}, DS_{133} (pre and post alien removal), DS_{135} and DS_{137}

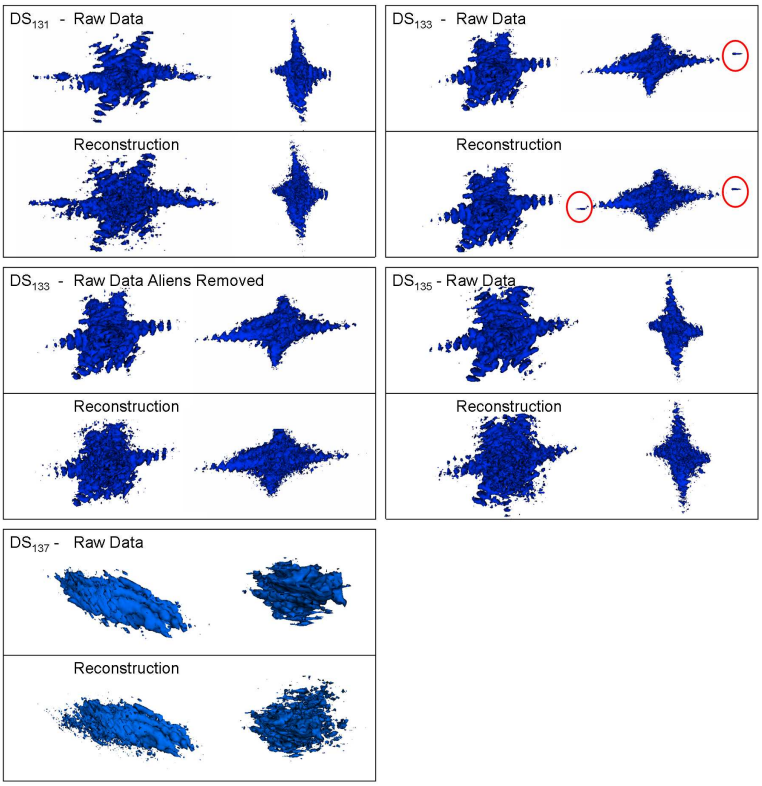

Figure 39: 3D renders of measured diffraction patterns and projected diffraction patterns from reconstructions of DS_{131}, DS_{133} (pre and post alien removal), DS_{135} and DS_{137}

be less than 100nm, we would expect to see an associated strain. This would exhibit as an expansion/contraction around the base not as an expansion on one side and contraction on the other as the phase suggests. A trait previously associated with centring, here the gradient of phase is not present across the whole reconstruction therefore is some form of inhomogenous strain.

The reconstruction of DS_{147} was very difficult, the support played a large role in limiting the reconstructed object. The presence of large amplitudes at the extremities of the support led to aliasing effects in the reconstructed diffraction pattern. A sharp edge in real space corresponds to high frequency oscillations (high resolution data) beyond the size of the defined support. The algorithms solution to this is to force all frequencies outside the array back onto itself, see figure 41. However the reconstruction of a phase structure was very encouraging to test that the result was actually consistent with the other datasets, the reconstructed solution was used as the starting point for the phasing of the other datasets. When the result is consistent with other datasets it should reconstruct a similar object and if the χ^2 is lower than the original failed reconstruction it is an improvement.

DS_{139} on its own did not reconstruct, with reconstruction solutions of $DS_{142/144}$ as starting points similar phase structures were maintained and the amplitude distribution improved. The χ^2 value was lowest for the original solution, suggesting stagnation, $142 < 144$. DS_{142} reconstructs a similar phase structure to that of DS_{144} when provided with DS_{144} as starting point higher but the χ^2 value was higher than its own solution. DS_{144} reconstructs a similar phase structure to that of DS_{142} when provided with DS_{142} as starting point higher but the χ^2 value was lower than its own solution. The conclusion from this is that DS_{142} is the correct reconstruction and the closest to the global minima. The phase maps for DS_{142} and DS_{144} are shown respectively in *Figures 42* and *43*.

As the data resolution is improved (400 accumulations) the ability too reconstruct smaller features means any space in the support becomes extremely important when constraining the algorithm. For example the support can be rotated to match the features of the object exactly, but must not interact with the reconstructed object, identified easily by aliasing in the reconstructed diffraction pattern and excessive amplitude outside of the support in direct space. Enhancement of the resolution costs the duration of a scan, an example of a high resolution datasets is shown in Figure 44, a total of 3 hours produced 16 resolvable fringes setting the resolution to 75nm across its width and 100nm along its length. Measurements of this length, require the sample to be heated to a temperature and cooled to a reference temperature and measured. This process ensures the phasing operation applied is consistent for all datasets and the reaction does not proceed during measurement.

Major problems with unique solutions have hampered the phasing of these datasets. The most encouraging reconstructions so far are shown in figure 45, the difference between the two is very small, asymmetry in the raw diffraction data may be the consequence of the crystal moving out of the beam during measurement, conclusive evidence for this has not been obtained.

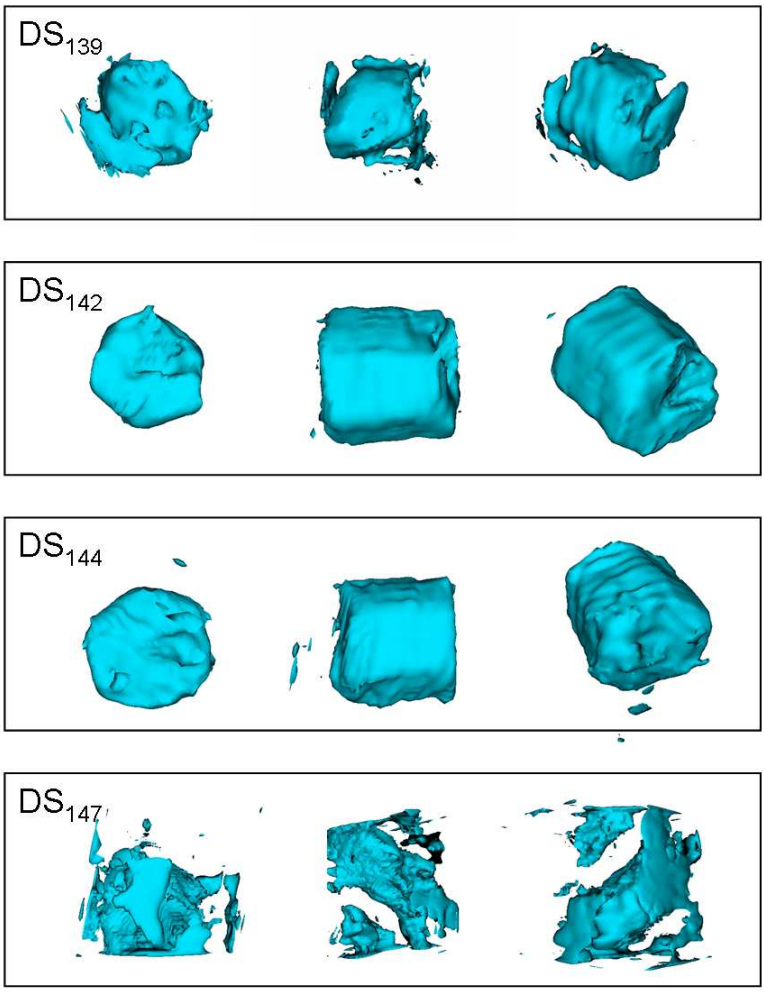

Figure 40: 3D renders of reconstructions for DS_{139}, DS_{142}, DS_{144} and DS_{147}

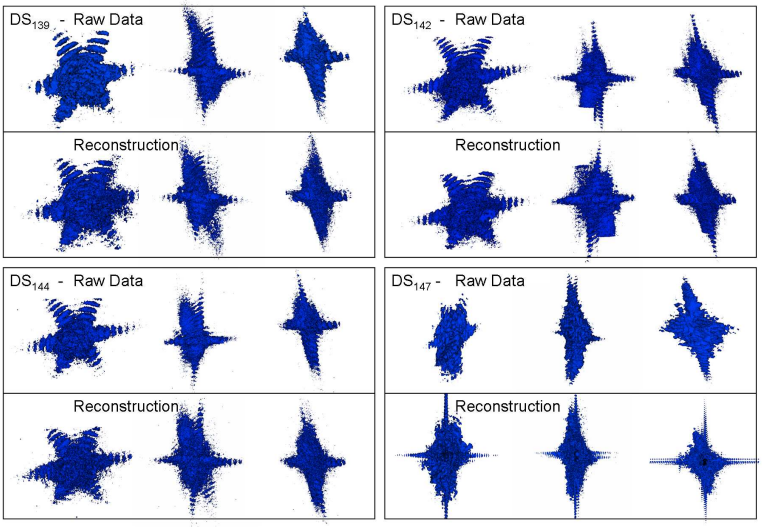

Figure 41: DS_{144} reconstruction, scalar cut planes taken through the phase along the Q vector and at subsequent 30° rotations

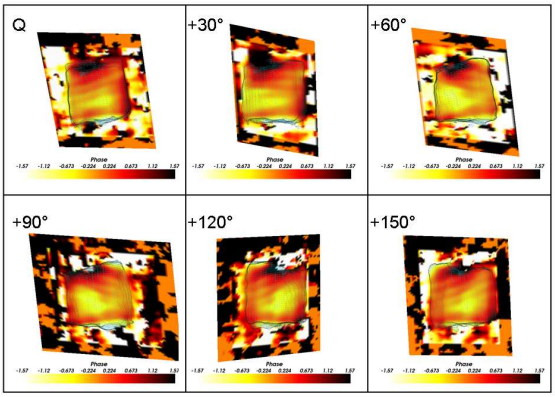

Figure 42: DS_{142} reconstruction, scalar cut planes taken through the phase along the Q vector and at subsequent 30° rotations

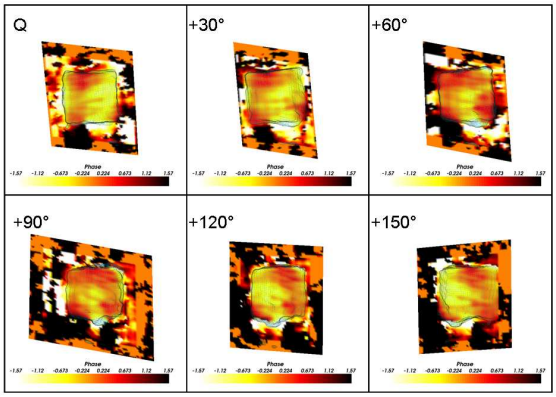

Figure 43: DS_{144} reconstruction, scalar cut planes taken through the phase along the Q vector and at subsequent 30° rotations

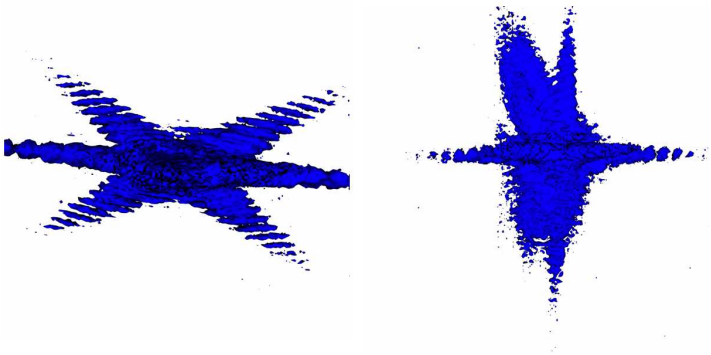

Figure 44: 3D render of diffraction data with 400 accumulations

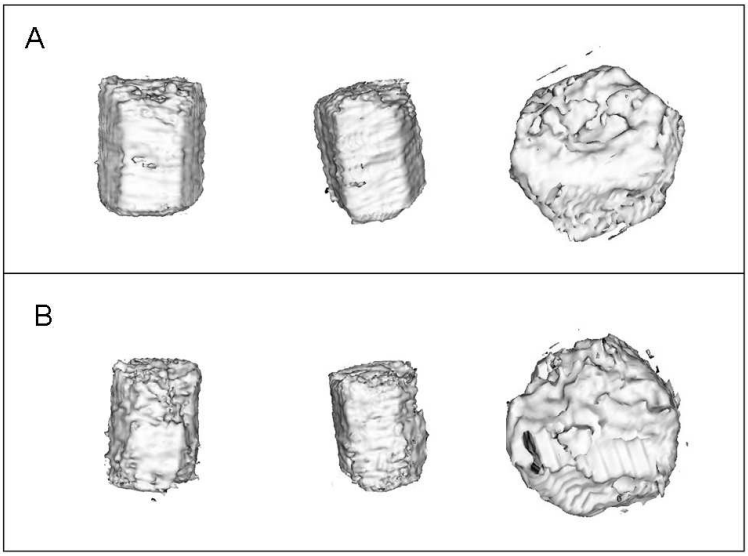

Figure 45: Preliminary reconstructions of DS_{54} at 292°C and DS_{64} at 402°C

4.3.5 Co

A single ZnO crystal was imaged with CXD before/after and upon annealing at 300°C, 350°C and 400°C for a cobalt deposition. The deposition thickness was visibly low but present as a blue tinge was observed, Dektak[5] proved inconclusive subsequent SEM images confirmed slight surface undulations suggesting deposition was achieved. The reconstructions are shown in Figure 46, here the phasing process involved 50 iterations of HIO followed by 50 iterations of ER starting from a copy of the support as a best guess for the object. The resolution is of the order 80nm along the length of the rod and 60nm across its facet. The undulations observed along the length of the rod are of the order of the resolution of the image so are unlikely to be real. All four datasets were centred and phased independently, to prevent errors associated with variables in the algorithms the datasets were embedded in identical arrays and phased with the same support. Therefore any variation in the reconstructed image are a property of the data alone. In this case fig.46D one facet of the crystal appears to be eaten away. This reduced amplitude suggests either the crystal no longer exists in this region or the strains created are so large it is beyond the capabilities of the algorithm to resolve. Note, the crystal was oriented perpendicular to the surface, a side on view is shown for the readers clarity.

4.3.6 Ni

Three Nickel depositions were carried out on ZnO crystals and they were tracked through annealing. Similar hurdles in the phasing algorithm mean they will not be included to avoid repetition.

[5]Veeco Dektak 8 profiler, London Centre for Nanotechnology Cleanroom Facilities

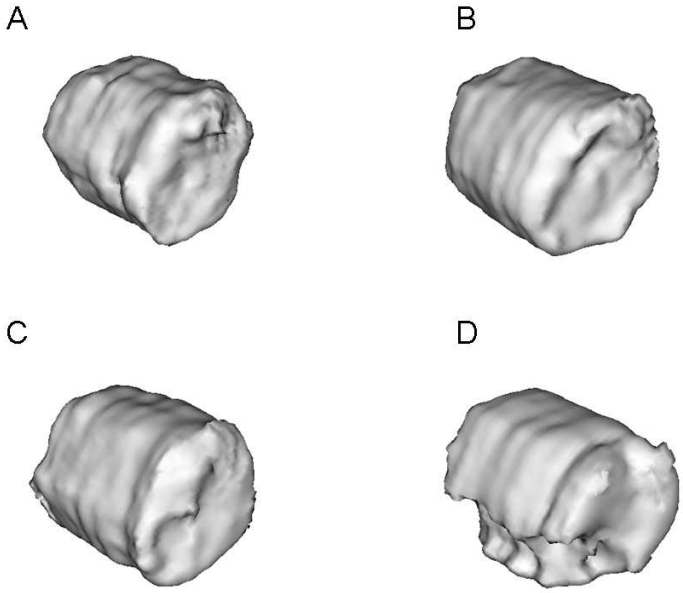

Figure 46: Reconstructions for sample 113 (A) before deposition DS (B) after deposition at 300°C DS (C) 350°C DS (D) 400°C DS

5 Conclusion

5.1 Zinc Oxide Nanocrystal Synthesis

The synthesis method has produced high yields of equiproportioned ZnO nanorods (up to 100%) loose on a substrate. A source material of Zinc Carbonate to Carbon weight ratio 10:1 heated to 900°C in an atmosphere of Argon (6.4% Oxygen) deposits ZnO nanorods on a substrate positioned at 150°C. The rod morphology was understood to be the result of the pressure maintained within the quartz tube. An accident has rendered the system unusable in the near future, upgrades will mean future experiments will require a recalibration to reproduce the results obtained.

5.2 Coherent X-ray Diffraction

It is clear there is no definitive phasing method for any particular dataset, to date attempts at phasing approximately 160 different datasets have identified no obvious advantage between specific algorithms. The general operation leads some form of HIO algorithm (30-50 iterations) to identify a solution followed by an a ER type algorithm (10-20) to clean up the result. The obvious advantage of the PC-HIO is the additional constraint when required and PO-ER allows amplitude to exist outside the support so provides a better representation of the noise in the data.

To achieve high resolution (a fifteenth of the size of the crystal) between two and four hundred accumulations are required to obtain sufficient statistics (>6 photons or 900 ADUs) in the outer fringes after threshold consideration. As the resolution is increased the support constraint becomes very important, large regions of empty space must be eradicated to find the unique solution.

The data processing has been advanced to a state whereby, a diffraction pattern can be measured and within an hour of acquisition a first rough reconstruction of the crystal can be achieved. A judgement on the quality of the crystal is possible for further measurements, i.e higher resolution analysis or in-situ measurements. The measurements obtained by Pfeifer and Williams on Au and Pb [34, 36] nanocrystals took up to 2 hours of equivalent exposure.

The uniqueness problem remains, from multiple random starting points algorithms are yet to produce >50% ambiguous solutions, suggesting the presence of many very similar local minima. This problem has been approached by Veit Elser [81] whereby each solution contains genuine features relating to the object. Multiple iterations are averaged to provide an overall average of the features present, those that occur more frequently will be prevalent in the final solution. This method could be implemented using cross correlations to overlay reconstructions.

When a crystal is tracked through some form of processing subtle variation in the diffraction patterns can be identified by phasing all datasets in the same way, using the same support, same phase constraint if there is one and when the crystal experiences the same conditions. This leaves all variation in the solution down to the difference in diffraction data alone, there maybe slight differences in centring so small gradients may be present but these have been reduced as much as possible. The in-situ measurements will incorporate this further by quenching after annealing to a reference state at which all measurements will

be made. Identifying the onset of the reaction is also very difficult, in a 3 hour scan a lot can change, the crystals change quickly and their behaviour varies slightly (temperature calibration etc). Two dimensional phasing has been used to try and identify variations around the Bragg peak, these proved unsuccessful due to thermal expansion making it very difficult to track and measure the same slice of the diffraction pattern.

As we have discovered from the multitude of solutions created from random starting points, *a priori* information is very important. It begs the question; How valid is a random starting point? The measurement around a Bragg peak suggests the crystal structure is not random, the application of a phase constraint adds weight to this argument, if the variation is small and it is constrained to be small the reconstructions improve. We have begun to apply this to diffraction patterns that should all exhibit similar features. Our previous solution should be the starting point for the next dataset, it is the most we know about the object and is a vast improvement on a random starting point. Obviously the unique nature of the original result remains questionable, it must be the global minimum to hold true. Alternately as shown in Section 4.3.4 by considering this fact we can back propagate solutions, i.e re run the previous dataset with the new datasets solution to try and justify the agreement between the reconstructions, here χ^2 becomes a very powerful tool at identifying which representation is indeed the most accurate representation of the data.

6 Outlook

6.1 Zinc Oxide Nanocrystal Synthesis

The degradation of ZnO nanostructures needs to be understood. The focus on ZnO growth should move toward a better control of the supersaturate and the nucleation of the nanostructures. Improved pressure control and catalysts could be used to achieve these goals, Indium is known to catalyse nanobelts over nanorod formation, *Fan et al. [68]* used Au catalyst to grow arrays of oriented nanowires and fields of randomly oriented nanobelts in the presence of In. *Gao et al. [69]* implemented Sn to grow ZnO nanowires using Metal-Organic Chemical Vapour Deposition (MOCVD). Synthesis of this nature will negate the need for surface adhesion although a surface interaction will result and provide a level of control for the manufacture of devices on a larger scale. This will also overcome degradation of the ZnO upon further growth of the silicon oxide layer. Early results using Energy Dispersive X-ray analysis (EDX) has shown Zn to be present in the grown oxide layer surrounding each crystal on the surface.

6.2 Coherent X-ray Diffraction

There are several avenues of investigation to pursue. The phase retrieval algorithms need further development, to cope with scenarios in which phase 'wraps' with variations in excess of 2π, to improve the reproducibility of solutions obtained from random starting points in order to overcome the unique solution problem. Errors in data collection must also be addressed, for example the error on the ADU measurement of the intensity (I) by the CCD is not considered, $\sqrt{I}$.

Further experiments are to be carried out on decomposition of ZnO with transition metals, a greater control over the experimental process is required. The sample will be annealed to 400 degrees for several minutes and quenched to a known stable temperature of 300 degrees where it will be measured and the process repeated until decomposition is observed. The individual measurements require 3 hour scans for sufficient statistics to obtain sub 75nm resolution for larger crystals.

The illumination of multiple crystals on a sample surface makes it difficult to orient a single crystal in the beam and measure multiple Bragg peaks. The question of structural displacements in three dimensions becomes a reality if a single crystal can be oriented on the surface, illuminated and the subsequent diffraction measured. This has been achieved by Robinson *et al.*, the data is in the analysis stage and was taken from a single ZnO rod placed on silicon substrates with a micromanipulator, oriented roughly using SEM characterisation and fully with a Laue orientation matrix [82], at beamline 34-ID-E at the APS. The sample was then oriented on the 34-ID-C beamline and after some laborious searching in reciprocal space multiple Bragg peaks were measured.

This advance in the technique means a direct measurement of the diffracting crystal has been made using SEM and provides very detailed *a priori* knowledge of the support for phasing the diffraction data. A favoured method for the fabrication of electronic devices on this lengthscale is the Focussed Ion Beam (FIB); a focused beam of Gallium ions is used to deposit metals and mill devices on the nanoscale with beams of the 4nm order. It is well known irradiation of this nature induces defects in materials [83–85], ultimately these defects will change the physical properties of the materials, the extent of which can be imaged using CXD. Strains induced by device operation could also be investigated in this manner.

The coherence properties of the beam is a major concern for the larger crystal experiments; specifically the longitudinal coherence in the unfocussed setup and both the transverse and longitudinal coherence in the focussed setup. The inability of algorithms to reconstruct diffraction patterns with a combination of interference and addition present in the intensity distribution is expected and near impossible, data obtained in this way is not useless and will effectively lead to projections of crystal structures in the dimension of the lack of coherence. Whether this is in fact a useful property remains to be seen. The coherence properties of illumination for CXD has been investigated by the author in the attached article 'Longitudinal Coherence Function of a Third Generation Synchrotron Beamline'. There needs to be a distinction between an incoherent diffraction pattern and an undersampled dataset; a coherent diffraction pattern maybe undersampled and will appear incoherent but is potentially phaseable [22], however full reconstructions in 3D from incoherent data are almost inconceivable. This challenges the notion that a dataset with an overall oversampling ratio of 2 can be reconstructed and finds a ratio of 2 is in fact required in every dimension.

References

[1] J. A. Pitney. Coherent x-ray diffraction. *Thesis*, 2000.

[2] G. J. Williams. Microscopy of gold microcrystals by coherent x-ray diffractive imaging. *Thesis*, 2005.

[3] M. A. Pfeifer. Structural studies of lead nanocrystals using coherent x-ray diffraction. *Thesis*, 2005.

[4] D. Sayre J. Miao and H. N. Chapman. Phase retrieval from the magnitude of the fourier transforms of nonperiodic objects. *J. Opt. Soc. Am. A*, 15(6):1662–1670, 1998.

[5] I. K. Robinson. Direct determination of the au(110) reconstructed surface by x-ray diffraction. *Phys. Rev. Lett.*, 50(15):1145–1148, 1983.

[6] J. R. Fienup. Reconstruction of a complex-valued object from the modulus of its fourier transform using a support constraint. *J. Opt. Soc. Am. A*, 4(1):118–123, 1987.

[7] J. R. Fienup. Phase retrieval algorithms a comparison. *Applied Optics*, 21(15):2758–2769, 1980.

[8] Synthesis and characterisation of zinc oxide tetrapod nanocrystals. M. c. newton, s. firth, t. matsuura and p. a. warburton. *J. Phys: Conf. Series*, 26:251–255, 2006.

[9] Y. J. Xing et al. Thermal evaporation synthesis of zinc oxide nanowires. *Appl. Phys. A*, 80:1527–1530, 2003.

[10] W. C. Roentgen. On a new kind of rays. *Nature*, 53(1369):274–276, 1896.

[11] J. Als-Nielsen and D. McMorrow. Elements of modern x-ray physics. *WILEY*, page 25, 2001.

[12] F. van der Veen and F. Pfeiffer. Coherent x-ray diffraction. *J. Phys Cond. Matt.*, 16:5003–5030, 2004.

[13] I. K. Robinson. Crystal truncation rods and surface roughness. *Phys. Rev. B*, 33(6):3830–3836, 1986.

[14] C. A. Kenney-Benson I. K. Robinson and I. A. Vartanyants. Sources of decoherence in beamline optics. *Physica. B*, 336:56–62, 2003.

[15] D. Sayre. Some implications of a method by shannon. *Acta Cryst.*, 5:843, 1952.

[16] R. P. Millane. Phase retrieval in crystallography and optics. *J. Opt. Soc. Am. A.*, 7:394–411, 1990.

[17] R. Barakat and G. Newsam. Necessary conditions for a unique solution to two dimensional phase recovery. *J. Math. Phys.*, 25:3190–3193, 1984.

[18] R. W. Gerchberg and W. O. Saxton. A practical algorithm for the determination of phase from image and diffraction plane pictures. *Optik*, 35:237–246, 1972.

[19] J. R. Fienup. Reconstruction of an object from the modulus of its fourier transform. *Optics Letters*, (3):27–29, 1978.

[20] S. Marchesini. A unified evaluation of iterative projection algorithms for phase retrieval. *Rev. Sci. Instruments*, 78(011301):1–10, 2007.

[21] R. Harder. Discussions.

[22] R. P. Millane and W. J. Stroud. Reconstructing symmetric images from their undersampled fourier intensities. *J. Opt. Soc. Am. A*, 14(3):568–579, 1997.

[23] C. W. Wang C-C. Chen, J. Miao and T. K. Lee. Application of optimization technique to noncrystalline x-ray diffraction microscopy: Guided hybrid input-output method. *Phys. Rev. B*, 76(064113), 2007.

[24] J. P. Abrahams and A. G. W. Leslie. Methods used in the structure determination of bovine mitochondrial f1 atpase. *Acta. Crystallography D*, 52:30–42, 1996.

[25] V. Elser. Phase retrieval by iterated projections. *J. Opt. Soc. Am*, 20(1):40–55, 2003.

[26] P. L. Combettes H. H. Bauschke and D. R. Luke. Phase retrieval, error reduction algorithm and fienup variants: a view from complex optimization. *J. Opt. Soc. Am*, 19(7):1334–1345, 2002.

[27] P. L. Combettes H. H. Bauschke and D. R. Luke. n. *J. Opt. Soc. Am*, 20, 2003.

[28] D. R. Luke. Relaxed average alternating reflections for diffraction imaging. *Inverse Problems*, 21:37–50, 2005.

[29] J. R. Fienup and C. C. Wackerman. Phase-retrieval stagnation problems and solutions. *J. Opt. Soc. Am. A*, 3(11):1897–1907, 1986.

[30] H. N. Chapman S. P. Hau-Riege A. Noy M. R. Howells U. Weierstall S. Marchesini, H. He and J. C. H. Spence. X-ray image reconstruction from a diffraction pattern alone. *Physical Review B*, 68(140101):1–4, 2003.

[31] J. Kirz J. Miao, P. Charalambous and D. Sayre. Extending the methodolgy of x-ray crystallography to allow imaging of micrometre-sized noncrystalline specimens. *Nature*, 400:342–344, 1999.

[32] G. J. Williams M. A. Pfeifer I. K. Robinson, I. A. Vartanyants and J. A. Pitney. Reconstruction of the shapes of gold nanocrystals using coherent x-ray diffraction. *Phys. Rev. Lett.*, 87(19), 2001.

[33] J. Miao et al. High resolution 3d x-ray diffraction microscopy. *Phys. Rev. Lett.*, 89(8), 2002.

[34] I. A. Vartanyants G. J. Williams, F. Pfeiffer and I. K. Robinson. Three-dimensional imaging of microstructure in au nanocrystals. *Phys. Rev. Lett.*, 90(17), 2003.

[35] I. A. Vartanyants G. J. Williams, M. A. Pfeifer and I. K. Robinson. Internal structure in small au crystals resolved by three-dimensional inversion of coherent x-ray diffraction. *Phys. Rev. B*, 73:0941121, 2006.

[36] I. A. Vartanyants R. Harder M. A. Pfeifer, G. J. Williams and I. K Robinson. Three-dimensional mapping of a deformation field inside a nanocrystal. *Nature*, 442:63–66, 2006.

[37] G. J. Williams I. A. Vartaniants R. Harder, M. A. Pfeifer and I. K. Robinson. Orientation variation of surface strain. *phys. Rev. B.*, 76(115425):1–4, 2007.

[38] C. Song B. Amirbekian Y. Kohmura Y. Nishino Y. Takahashi T. Ishikawa H. Jiang, D. Rammuno-Johnson and J. Miao. Nanoscale imaging of mineral crystals inside biological composite materials using x-ray diffraction microscopy. *Phys, Rev. Lett.*, 100(038103):1–4, 2008.

[39] G. J. Williams J. N. Clark A. G. Peele M. A. Pfeifer M. de Jonge B. Abbey, K. A. Nugent and I. McNulty. Keyhole coherent diffractive imaging. *Nature Physics*, pages 1–5, 2008.

[40] H. N. Chapman C. Cui M. R. Howells D. A. Shapiro A. M. Minor J. C. H. Spence U. Weierstall J. Ilavsky A. Noy S. P. Hau-Riege A. B. Artyukhin T. Baumann T. Wiley J. Stolken T. van Buuren A. Barty, S. Marchesini and J. H. Kinney. Three-dimensional coherent x-ray diffraction imagin of a ceramic nanofoam: determination of structural deformation mechanisms. *arXiv: cond-matt.mtrl-sci*, 1(0708.4035):1–5, 2007.

[41] J. M. Zuo. Atomic resolution imaging of a carbon nanotube from diffraction intensities. *Science*, 300:1419–1421, 2003.

[42] T. Fujita and M. R. McCartney. Phase recovery for electron holography using gerchberg-papoulis iterative algorithm. *Ultramicroscopy*, 102:279–286, 2005.

[43] R. Koster V. Favre-Nicolin, J. Eymery and P. Gentile. Coherent diffraction imaging of single 95nm nanowires. *Arxiv.org*, 2008.

[44] S. Labat B. Mandl R. T. Lechner V. Chamard, J. Stangl and T. H. Metzger. Evidence of stacking-fault distribution along an inas nanowire using microfocused coherent x-ray diffraction. *J. Appl. Cryst*, 41:272–280, 2008.

[45] J-S. MIcha B. Charlet V. Chamard A. A. Minkevich, M. Gailhanou and O. Thomas. Inversion of the diffraction pattern from an inhomogeneously strained crystal using an iterative algorithm. *Physical Review B*, 76(104106):1–5, 2007.

[46] C. G. Schroer et al. Coherent x-ray diffraction imaging with nanofocused illumination. *Phys. Rev. Lett.*, 101:090801–4, 2008.

[47] J. M. Rodenburg and H. M. L Faulkner. A phase retrieval algorithm for shifting illumination. *Appl. Phys. Lett.*, 85(20), 2004.

[48] H. M. L. Faulkner and J. M. Rodenburg. Movable aperture lensless transmission microscopy:a novel phase retrieval algorithm. *Phys. Rev. Lett.*, 93(2), 2004.

[49] A. Menzel-O. Bunk C. David P. Thibault, M. Dierolf and F. Pfeiffer. High resolution scanning x-ray diffraction microscopy. *Science*, 321(379), 2008.

[50] T. Beetz-V. Elser M. Howells C. Jacobsen J. Kirz E. Lima H. Miao A. M. Neiman D. Shapiro, P. Thibault and S. Sayre. Biological imaging by soft x-ray diffraction microscopy. *PNAS*, 102(43):15343–15346, 2005.

[51] W. Schlotter-M. Lorgen O. Hellwig W. Eberhardt andJ. Stohr S. Eisebitt, J. Luning. Direct holographic inversion 1.59nm rcp diffraction from magnetised film and pinhole. *Nature*, 432:885–888, 2004.

[52] M. J. Bogan S. Boutet M. Frank S. P. Hau-Riege S. Marchesini B. W. Woods S. Bajt W. Henry Benner R. A. London E. Plonjes-M. Kuhlmann R. Treusch S. Dusterer T. Tschentscher J. R. Schneider E. Spiller T. Moller C. Bostedt M. Hoener D. A. Shapiro K. O. Hodgson D. van der Spoel F. Burmeister M. Bergh C. Caleman G. Huldt M. Marvin Seibert F. R. N. C. Maia R. W. Lee A. Szoke N. Timneanu H. N. Chapman, A. Barty and J. Hajdu. Femtosecond diffractive imaging with a soft-x-ray free-electron laser. *arXiv:physics/0610044v2*, pages 1–6, 2006.

[53] M. J. Bogan S. Bajt A. Barty S. Boutet S. Marchesini M. Frank B. W. Woods W. H. Benner R. A. London U. Rohner-A. Szoke E. Spiller T. Moller C. Bostedt D. A. Shapiro M. Kuhlmann R. Treusch E. Plonjes F. Burmeister M. Bergh C. Caleman G. Huldt M. M. Seibert H. N. Chapman, S. P. Hau-Riege and J. Hajdu. Femtosecond time-delay x-ray holography. *Nature*, 448:676–680, 2007.

[54] I. McNulty C. David P. Wochner I. A. Vartanyants, I. K. Robinson and Th. Tschentscher. Coherent x-ray scattering and lensless imaging at the european xfel facility. *J. Synchrotron Rad.*, 14:453–470, 2007.

[55] X. Wang Y. Qin and Z. L. Wang. Microfibre-nanowire hybrid structure for energy scavenging. *Nature*, 451:809–814, 2008.

[56] Z. L. Wang. Zinc oxide nanostructures: growth, properties and applications. *J. Phys. Cond. Matt.*, 16:R829–R858, 2004.

[57] Z. L. Wang. Nanostructures of zinc oxide. *Materials Today*, pages 26–33, 2004.

[58] M. Newton. Zinc oxide tetrapod nanocrystal diodes. *Thesis*, 2007.

[59] Y. Ding and Z. L. Wang. Zinc blende zno and its role in nucleating wurtzite tetrapods. *Microscopy Society of America*, 13(2), 2007.

[60] M. Newton and P. Warburton. Zinc oxide tetrapod nanocrystals. *Materials Today*, 10(5), 2007.

[61] A. Meisel E. C. Scher L. Manna, D. J. Milliron and P. A. Alivisatos. Controlled growth of terapod-branched inorganic nanocrystals. *Nature Materials*, 2:382–385, 2003.

[62] C. Wang G. Yi and W. Park. Zno nanorods: synthesis, characterization and applications. *Semicond. Sci. Technol.*, 20:S22–S34, 2005.

[63] L. Liao et al. Size dependence of gas sensitivity of zno nanorods. *J. Phys. Chem.*, 111:1900–1903, 2007.

[64] M. A. Zimler J. Bao and F. Capasso. Broadband zno single-nanowire light-emitting diode. *Nano Letters*, 6(8):1719–1722, 2006.

[65] X. Zhang S. A. Dayeh D. P. R. Aplin C. Soci D. Yu B. Xiang, P. Wang and D. Wang. Rational synthesis of p-type zinc oxide nanowire arrays using simple chemical vapor deposition. *Nano. Lett.*, 7(2), 2006.

[66] Y. Zhang Y. Dai and Z. L. Wang. Synthesis and optical properties of tetrapod-like zinc oxide nanorods. *Solid State Comm.*, 126:629–633, 2003.

[67] Y. F. Chan B. D. Yao and N. Wang. Formation of zno nanostructures by a simple way of thermal evaporation. *Appl. Phys. Lett.*, 81(4):757–759, 2002.

[68] R. Scholz C. Himcinschi A. Berger H. Leipner A. Dadgar A. Krost S. Christiansen U. Gosele H. J. Fan, B. Fuhrmann and M. Zacharias. Vapour-transport-deposition growth of zno nanostructures: switch between c-axial wires and a-axial belts by indium doping. *Nanotechnology*, 17:S231–S239, 2006.

[69] Y. Ding P. X. Gao and Z. L. Wang. Crystallographic orientation-aligned zno nanorods grown by a tin catalyst. *Nano Lett.*, 3(9):1315–1320, 2003.

[70] J. Y. Zhang D. Z. Shen Y. M. Lu Y. C. Liu X. Q. Meng, D. X. Zhao and X. W. Fan. Growth temperature controlled shape variety of zno nanowires. *Chem. Phys. Lett.*, 407:91–94, 2005.

[71] M. Howells U. Weierstall G. Hembree H. He, S. Marchesini and H. Spence. Experimental lensless soft x-ray imaging using iterative algorithms: phase diffuse scattering. *Acta Crystallographica A*, 59:143–152, 2003.

[72] S. Marchesini A. Noy S. P. Hau-Riege C. Cui M. R. Howells R. Rosen H. He J. C. H. Spence U. Weierstall T. Beetz C. Jacobsen H. N. Chapman, A. Barty and D. Shapiro. High-resolution ab initio three-dimensional x-ray diffraction microscopy. *J. Opt. Soc. Am. A*, 23(5):1179–1200, 2006.

[73] Steve B. Howell. Handbook of ccd astronomy. *Cambridge University Press*, 2006.

[74] L. Pauling. The nature of the chemical bond. *Cornell University Press*, 1960.

[75] A. A. Allred. *J. Inorg. Nucl. Chem.*, 17(215), 1961.

[76] T. Fukumura M. Kawasaki K. Ando H. Saito T. Sekiguchi-Y. Z. Yoo M. Murakami Y. Matsumoto T. Hasegawa Z, Jin and H. Koinuma. High throughput fabrication of transition-metal-doped epitaxial zno thin films: A series of oxide-diluted magnetic semiconductors and their properties. *Appl. Phys. Lett.*, 78(24):3824–3826, 2001.

[77] A. W. Sleight R. Wang and M. A. Subramanian. An unusual iron site in iron-doped zinc oxide. *Journal of Solid State Chemistry*, 125:224–227, 1996.

[78] K. W. Geng F. Zeng B. He X. X. Wei, C. Song and F. Pan. Local fe structure and ferromagnetism in fe-doped zno films. *J. Phys.: Condens. Matter*, 18:7471–7479, 2006.

[79] W. B. White C. H. Bates and R. Roy. The solubility of transition metal oxides in zinc oxide and the reflectance spectra of mn2+ and fe2+ in tetrahedral fields. *J. Inorg. Nucl. Chem.*, 28:397–405, 1966.

[80] J-S. Micha B. Charlet A. A. Minkevich-R. Fortunier M. Gailhanou, A. Loubens and O. Thomas. Strain field in silicon on insulator lines using high resolution x-ray diffraction. *Appl. Phys. Lett.*, 90(111914):1–3, 2007.

[81] V. Elser. Reconstruction of an object from its symmetry-averaged diffraction pattern. *Acta Crystallographica Section A*, pages 1–9, 2005.

[82] W. Liu. Discussion.

[83] K. Gamo S. Takaoka T. Yamamoto, J. Yanagisawa and K. Murase. Estimation of damage induced by focused ga ion beam irradiation. *Japanese Journal of Applied Physics*, 32(12B):6268–6273, 1993.

[84] E. Bellingeri A.S. Siri D. Marr I. Pallecchi, L. Pellegrino and G.C. Gazzadi. Investigation of fib irradiation damage in la0.7sr0.3mno3 thin films. *Journal of Magnetism and Magnetic Materials*, 320(13):1945 – 1951, 2008.

[85] J. Zhang J. Yu, J. Liu and J. Wu. Tem investigation of fib induced damages in preparation of metal material tem specimens by fib. *Materials Letters*, 60(2):206 – 209, 2006.